

Calorimetry at a Future Linear Collider

Steven Green
of Emmanuel College

A dissertation submitted to the University of Cambridge
for the degree of Doctor of Philosophy

Abstract

This thesis describes the optimisation of the calorimeter design for collider experiments at the future Compact LInear Collider (CLIC) and the International Linear Collider (ILC). The detector design of these experiments is built around high-granularity Particle Flow Calorimetry that, in contrast to traditional calorimetry, uses the energy measurements for charged particles from the tracking detectors. This can only be realised if calorimetric energy deposits from charged particles can be separated from those of neutral particles. This is made possible with fine granularity calorimeters and sophisticated pattern recognition software, which is provided by the PandoraPFA algorithm. This thesis presents results on Particle Flow calorimetry performance for a number of detector configurations. To obtain these results a new calibration procedure was developed and applied to the detector simulation and reconstruction to ensure optimal performance was achieved for each detector configuration considered.

This thesis also describes the development of a software compensation technique that vastly improves the intrinsic energy resolution of a Particle Flow Calorimetry detector. This technique is implemented within the PandoraPFA framework and demonstrates the gains that can be made by fully exploiting the information provided by the fine granularity calorimeters envisaged at a future linear collider.

A study of the sensitivity of the CLIC experiment to anomalous gauge couplings that effect vector boson scattering processes is presented. These anomalous couplings provide insight into possible beyond standard model physics. This study, which utilises the excellent jet energy resolution from Particle Flow Calorimetry, was performed at centre-of-mass energies of 1.4 TeV and 3 TeV with integrated luminosities of 1.5ab^{-1}

and $2ab^{-1}$ respectively. The precision achievable at CLIC is shown to be approximately one to two orders of magnitude better than that currently offered by the LHC.

In addition, a study into various technology options for the CLIC vertex detector is described.

Declaration

This dissertation is the result of my own work, except where explicit reference is made to the work of others, and has not been submitted for another qualification to this or any other university. This dissertation does not exceed the word limit for the respective Degree Committee.

Steven Green

Acknowledgements

Of the many people who deserve thanks, some are particularly prominent, such as my supervisor . . .

Contents

1 Particle Flow Calorimetry for Future Linear Colliders	1
1.1 Particle Flow Calorimetry	1
1.2 International Large Detector	4
1.2.1 Overview	4
1.2.2 Vertex Detector	5
1.2.3 Time Projection Chamber	6
1.2.4 Supplemental Silicon Tracking System	7
1.2.5 Electromagnetic Calorimeter	10
1.2.6 Hadronic Calorimeter	11
1.2.7 Solenoid, Yoke and Muon System	13
1.2.8 Forward Calorimetry	14
1.3 Simulation	16
1.4 CLIC ILD	17
1.5 Particle Flow Reconstruction	18
1.5.1 PandoraPFA	19
1.6 Performance	21
1.6.1 Jet Energy Resolution	22
1.6.2 Decomposition of the Jet Energy Resolution	25
1.6.3 Single Particle Energy Resolution	27
1.7 Summary of ILD Detector Performance	28
2 The Sensitivity of CLIC to Anomalous Gauge Couplings through Vector Boson Scattering	33
2.1 Motivation	33
2.2 Event Generation, Simulation and Reconstruction	37
2.3 Modelling of Anomalous Gauge Couplings	39
2.4 Data Analysis	42
2.4.1 Limiting Beam Related Backgrounds	42

2.4.2	Jet Finding	42
2.4.2.1	Optimal Jet Finding Algorithm	45
2.4.3	Lepton Finding	47
2.4.4	Discriminant Variables	47
2.4.5	Jet Energy Resolution at CLIC	48
2.5	Event Selection	49
2.5.1	Preselection	50
2.5.2	Multivariate analysis	50
2.5.3	Event Selection Summary	54
2.6	Anomalous Coupling Fitting Methodology	54
2.6.1	Sensitive Distribution	54
2.6.2	χ^2 Surface and Confidence Limit Definition	57
2.6.3	Event Weight Interpolation Scheme	59
2.7	Results	60
2.7.1	Systematic Uncertainties	60
2.8	Sensitivity for $\sqrt{s} = 3$ TeV	64
	Bibliography	73

*“Writing in English is the most ingenious torture
ever devised for sins committed in previous lives.”*

— James Joyce

Chapter 1

Particle Flow Calorimetry for Future Linear Colliders

“I am fond of pigs. Dogs look up to us. Cats look down on us. Pigs treat us as equals.”

— Winston Churchill

Particle flow calorimetry can provide extremely good jet energy resolutions at a future linear collider. Jet energy resolution is crucial at the linear collider as many of the interesting processes will be characterised by multi-jet final states. Many of these multi-jet final states will be produced from the hadronic decays of W and Z bosons and one of the key goals of the future linear collider is to be able to separate these decays. Separation of these decays can be achieved, however, only by placing a tight requirement on the jet energy resolution; $\sigma_E/E \lesssim 3.5\%$ for 50-500 GeV jets at the ILC and up to 1.5 TeV at CLIC [1]. The use of particle flow calorimetry will also be highly beneficial for quantifying final states of interest that involving charged leptons and missing momentum.

1.1 Particle Flow Calorimetry

The premise of particle flow calorimetry is to use the sub-detector that offers the best energy resolution to measure the energy of any given particle, which corresponds to energy measurements being made in the ECal for γ s, the HCal for neutral hadrons and, crucially, the tracker for charged particles. The starker contrast of this approach to that

of traditional calorimetry occurs in the measurement of the energy of charged particles. In particle flow calorimetry the energy of a charged particle is measured using the curvature of the path it transverses as it bends in a magnetic field, while in traditional calorimetry the energy would be measured using the calorimeters, predominantly the hadronic calorimeter (HCal). The tracker energy resolution for a single charged particle of energy E_{X^\pm} is typically $10^{-4} \times E_{X^\pm}^2$, while for the HCal it is $\sim 0.55 \times \sqrt{E_{X^\pm}}$ [1]. The energy resolution offered by the tracker is significantly better than that offered by the HCal for energies up to $\sim \mathcal{O}(300 \text{ GeV})$. This means that particle flow calorimetry has the potential to offer a much better energy resolution for charged particles below $\sim \mathcal{O}(300 \text{ GeV})$, than that of the traditional calorimetry approach. Particle flow calorimetry offers gains in performance for collision energies well beyond 300 GeV as the average long-lived particle energy for physics processes of interest is typically much less than 300 GeV. Furthermore, it also leads to a significant improvement in the measurement of jet energies as, after the decay of short-lived particles, approximately 60% of the energy of a jet is carried in the form of charged particles. The measurement of jet energies in the particle flow paradigm is summarised in table 1.1. The benefits to the energy resolution, for both charged particles and jets, offered by the particle flow approach to calorimetry is the driving factor behind why it is planned for used at the linear collider experiment.

Jet Component	Detector	Energy Fraction	Energy Resolution
Charged Particles (X^\pm)	Tracker	$\sim 0.6E_j$	$10^{-4} \times E_{X^\pm}^2$
Photons (γ)	ECal	$\sim 0.3E_j$	$0.15 \times \sqrt{E_\gamma}$
Neutral Hadrons (X^0)	HCal	$\sim 0.1E_j$	$0.55 \times \sqrt{E_{X^0}}$

Table 1.1: The approximate jet fractions and energy resolutions for charged particles (X^\pm) of energy E_{X^\pm} , photons (γ) of energy E_γ and neutral hadrons (X^0) of energy E_{X^0} . The energy resolution for photons and neutral hadrons reflects the performance of a linear collider like ECal and HCal respectively. Taken from [1].

Particle flow calorimetry is challenging to put into practice as it requires a precise reconstruction for all long-lived particles within a detector. Charged particle energy measurements are made using the curvature of the track they transverse as they bend in the magnetic field, but they also produce calorimetric energy deposits, as shown in figure 1.1. If both of these energy measurements are used, the energy of all charged particles would be double counted. Therefore, to avoid this, any calorimetric energy deposits originating from charged particles are not included in the final energy measurement. However, this

methodology makes it possible to double count and omit energy measurements if the origin of a calorimetric energy deposit is misidentified. For example:

- If a calorimetric energy deposit, made by a charged particle, is not associated to a track, the calorimetric energy deposit will be double counted: Firstly, when the track energy is accounted for and secondly, when the calorimetric energy deposit is incorrectly reported as the energy of a neutral particle.
- If a calorimetric energy deposit, made by a neutral particle, is incorrectly associated to a track, that calorimetric energy deposit is not accounted for.

These effects, collectively known as "confusion", degrade the energy resolution of a particle flow detector. Therefore, it is crucial to make correct associations between charged particle tracks and their calorimetric energy deposits to minimise the effect of confusion. These associations can only be successfully made if the calorimeters used have fine segmentation, such as those found at the linear collider experiment, so that it becomes possible to separate the energy deposits from nearby showering particles. Even with this segmentation, making the association of charged particle tracks to calorimetric energy deposits is highly non-trivial. At the linear collider experiment, these associations are made using sophisticated pattern recognition algorithms, provided by PandoraPFA. The fine segmentation of the linear collider calorimeters allows PandoraPFA to reconstruct the four-momenta of all particles passing through the detector and to report the energy of all reconstructed particles using energy measurements from the optimal sub-detectors.

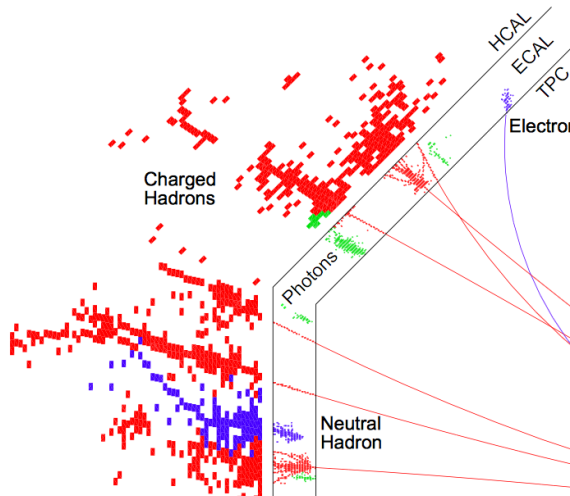


Figure 1.1: A typical simulated 250 GeV jet in the CLIC_ILD detector, with labels identifying constituent particles. Image taken from [2].

1.2 International Large Detector

The current detector concepts for the linear collider experiments have been designed to make particle flow calorimetry possible. While there are a number of different concepts that are under consideration for both the ILC and CLIC, one of the most prominent, and the focus of this work, is the International Large Detector (ILD). The ILD detector, shown in figure 1.2, achieves very high spatial resolution for all sub-detector systems thanks to its highly segmented calorimeters and central tracking system, both of which are encompassed within a 3.5 T magnetic field. The sophisticated pattern recognition software that is needed for particle flow calorimetry is provided by PandoraPFA [1, 2].

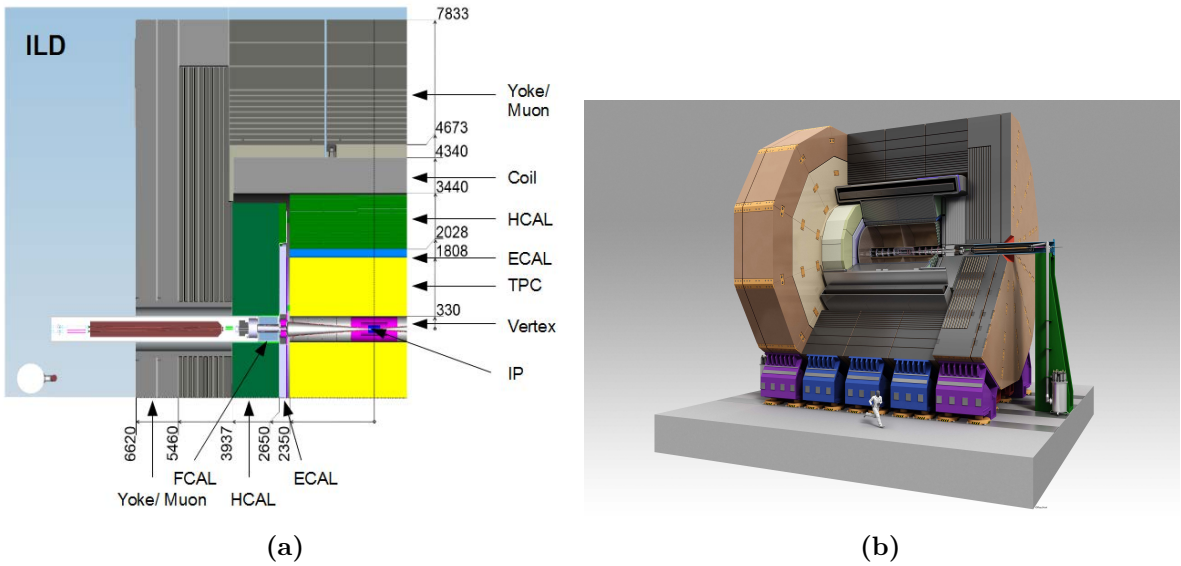


Figure 1.2: (a) Quadrant view of the ILD detector concept. The interaction point is in the lower right corner of the picture. Dimensions are in mm. (b) An artistic view of the ILD detector concept. Figures taken from [3].

1.2.1 Overview

The tracking system for the ILD detector consists of a vertex detector, a Time Projection Chamber (TPC) and a number of supplementary silicon detectors. The vertex detector is designed to give precise information about displaced vertices with respect to the impact point (IP), which is crucial for the study of short lived particles such as the D and B mesons. The vertex detector is located close to the IP and surrounding it is the TPC, which is the central tracker for ILD. The TPC provides detailed measurements of the

trajectory of charged particle tracks passing through it, up to 224 measurements per track. This information is used for determining the curvature of the charged particle track and hence the momentum of the charged particle that transversed it. Finally, the purpose of the supplementary silicon detectors is to provide additional, high precision, spatial measurements to aid track fitting and extend coverage of the detector down to low polar angles.

The calorimetric system for ILD is comprised of an electromagnetic calorimeter (ECal), a hadronic calorimeter (HCal) and a number of forward calorimeters (FCal). The primary function of the ECal is to induce electromagnetic particles to shower within it and to measure the energy of these particle showers. Similarly, the HCal is designed to induce and measure the energy of hadronic particle showers. The ECal surrounds the tracking system in the ILD detector and is itself surrounded by the HCal. The function of FCal is to extend the coverage of the calorimeter system to low polar angles and to provide measurements of the luminosity of the colliding e^\pm beams.

The outermost elements of the ILD detector are the solenoid, iron yoke and muon system. The solenoid generates a magnetic field of 3.5 T, which is essential for determining the energy of charged particles in the particle flow paradigm. The iron yoke is used to return the magnetic field generated by the solenoid. The yoke is instrumented by the muon system to provide additional information, which supplements the calorimetric energy measurements made by the ILD calorimeters.

1.2.2 Vertex Detector

The main goal of the ILD vertex detector is to achieve a resolution on the impact parameter of charged particle tracks of

$$\sigma_b < 5 \oplus \frac{10}{p \sin(\theta)^{3/2}} \mu\text{m}, \quad (1.1)$$

where σ_b is the resolution on the track impact parameter, p is the momentum of the track and θ is the angle between the track and the vertex detector plane. The first term in this parameterisation is the transverse impact parameters resolution and the second is a multiple-scattering term. This makes precisely tagging secondary vertices from charm and bottom mesons possible. Typically these mesons have relatively short proper lifetimes, τ , such that $c\tau \approx \mathcal{O}(300 \mu\text{m})$. To achieve this impact parameter resolution, a spatial resolution of better than 3 μm is required near the impact point (IP). Furthermore, a

low material budget of less than 0.15 % of a radiation length per layer is required to ensure that few electromagnetic showers are initiated within the vertex detector. A low pixel occupancy is essential for determining the trajectory of individual tracks in the detector. Furthermore, consideration will have to be given to the mechanical structure of the detector, power consumption and cooling.

There are a number of different pixel technology options under consideration for the vertex detector for the ILD detector. This is an active area of ongoing research and development for the linear collider collaboration. The current design of the vertex detector consists of three concentric layers of double-sided ladders with the first layer contains 10 ladders, the second 11 ladders and the third 17 ladders as shown in figure 1.3. Each ladder has two silicon pixel sensors on each side and the ladder thickness is approximately 2 mm. The radii covered by the detector range from 16 mm to 60 mm from the IP.

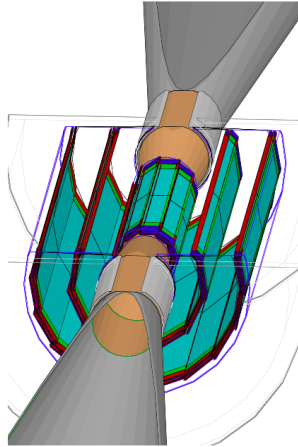


Figure 1.3: Vertex detector design for ILD. Figures taken from [4].

1.2.3 Time Projection Chamber

The central tracking system for the ILD detector is a TPC, which is shown in figure 1.4. The TPC consists of a cylindrical gas volume with a central electrode providing an axial electric field. When a charged particle passes through the TPC, it ionises the gas and the ionised molecules drift in the axial electric field. The direction of the electric field is chosen such that the electrons drift towards the endplates where they are collected. The position of the ionisation point can then be calculated using the drift time of the electrons in the TPC. Combining these TPC hits together makes reconstruction of the

full charged particle track possible. TPCs have an advantage over silicon tracking in that they continuously track any charged particle passing through them, while silicon detectors are only sensitive within each silicon layer. This compensates for the worse single point resolution that TPCs have in comparison to silicon detectors and makes TPCs a viable option for the ILD detector. Furthermore, TPCs have a very low material budget. This benefits calorimetry as it minimises energy losses prior to the particle energy entering the calorimeters, which means the calorimetric energy deposits give a better reflection of the true particle energy.

The ILD TPC has a point resolution of better than $100\ \mu\text{m}$ and a double hit resolution in ϕ of less than 2 mm. The gas used for the TPC will be Ar:CH₄:CO₂ (95:3:2) [4]. Several readout technology options, designed to measure the ionisation current, are currently under development. For all potential options it is envisaged that the readout pads would be $\approx 1 \times 6\text{mm}^2$ giving a total of approximately 10^6 pads on each TPC endplate.

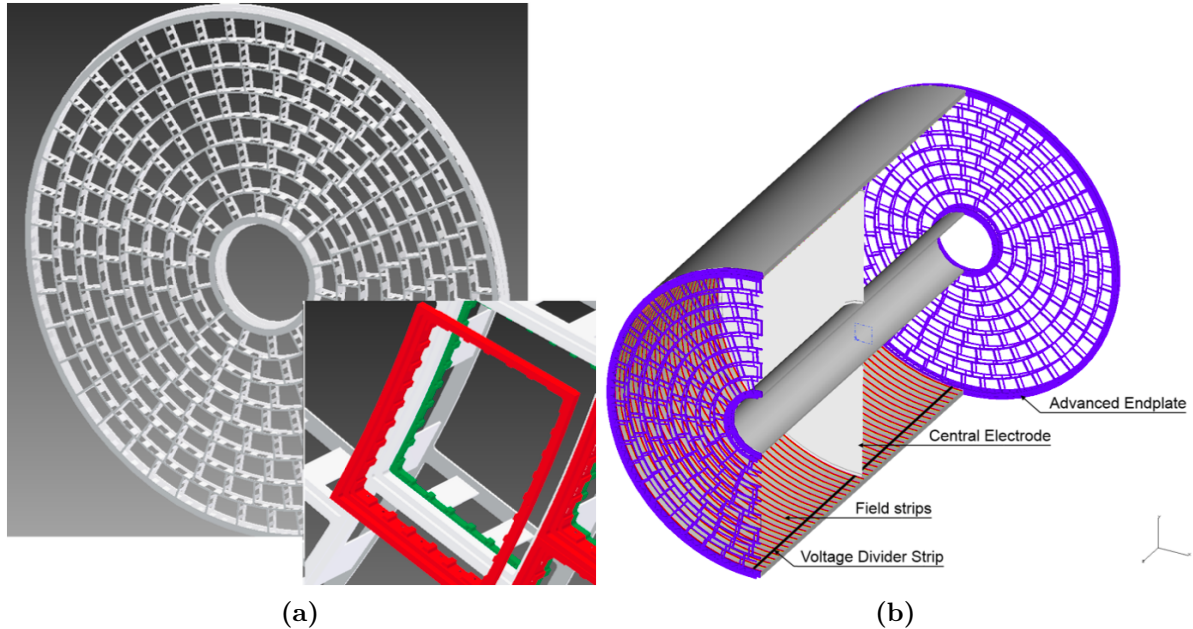


Figure 1.4: (a) Drawing of the proposed end-plate for the TPC. In the insert a back frame, which is designed to support the readout modules, is shown. (b) Conceptual sketch of the TPC system showing the main parts of the TPC (not to scale). The central electrode generates the axial electric field, the endplates collect the ionisation electrons, the field strips help to maintain a uniform electric field across the TPC and the voltage divider strips maintains the voltage difference between the anode and cathode. The field strips are held at fixed voltages such that they replicate the electric field produced by the electrodes. This reinforcing of the electric field configuration minimises non-uniformities in the electric field. The field cage of the TPC is not shown.

1.2.4 Supplemental Silicon Tracking System

There are four components that make up the supplemental silicon tracking system in ILD, shown in figure 1.5, which are:

- Silicon Inner Tracker (SIT) and Silicon External Tracker (SET). These are both barrel components, which are positioned immediately inside and outside the TPC. The SIT helps form associations between hits in the vertex detector and TPC, while the SET helps with extrapolation of TPC tracks into the calorimeter.
- Endplate of the TPC (ETD). This sensor is identical to the SET, but is positioned in front of the ECal endcap calorimeter. The ETD extends the coverage of the supplemental silicon tracking system envelope.
- Forward tracker (FTD). This detector consists of seven silicon disks that extend the coverage of the tracking down to small angles that are not covered by the TPC.

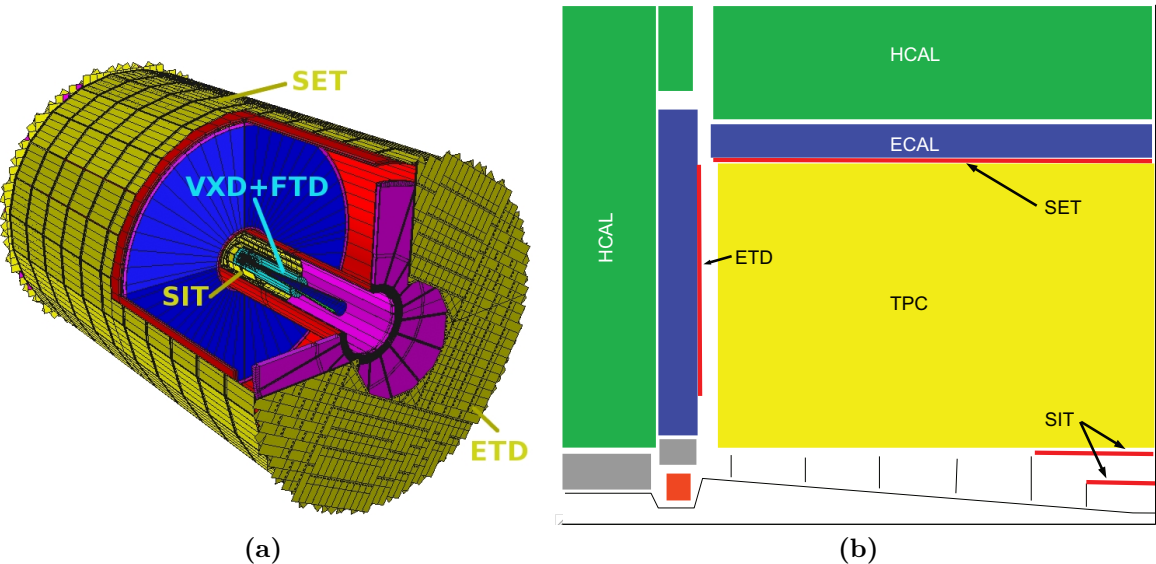


Figure 1.5: (a) A 3D detailed GEANT4 simulation description of the silicon system. (b) A quadrant view of the ILD silicon envelope made of the four components SIT, SET, ETD and FTD as included in the full MOKKA simulation. Figures taken from [3].

The coverage of the SIT, SET, ETD and FTD is given in table 1.2. These detectors are designed to give high precision space points that can be used in track fitting. Furthermore, the ETD and SET are of particular use for extrapolating the charged particle tracks into the calorimeters. This is key for particle flow calorimetry, which relies upon correct

Tracking System	Coverage [$\cos\theta$]
SIT	0.910
SET	0.789
ETD	0.799 - 0.985
FTD	0.802 - 0.996

Table 1.2: Coverage of the supplementary silicon tracking systems in the ILD detector. In this table θ is the polar angle with respect to the beam direction. Taken from [3].

association of charged particle tracks and clusters of calorimeter hits. Analogously to the vertex detector, these detectors require low material budget and low occupancy. The FTD, due to its proximity to the beam axis, is particularly prone to high occupancies.

The SIT, SET and ETD are silicon pixel sensors with $50 \mu\text{m}$ pitch embedded in $200 \mu\text{m}$ thick silicon. The FTD consists of seven silicon tracking disks, the first two being pixel detectors and the remaining five being strip detectors. The pixel detector disks are formed of 16 petals, as shown in figure 1.6. Within these petals the pixel size varies from $26 \times 29 \mu\text{m}^2$ to $26 \times 67 \mu\text{m}^2$. Strip detectors are used for the outermost tracking disks as the occupancy considerations do not demand a high granularity detector i.e. a pixel detector. These detector disks will have a pitch of $50 \mu\text{m}$. The active sensor and readout ASIC design for each of these detectors is an active area of development for the linear collider.

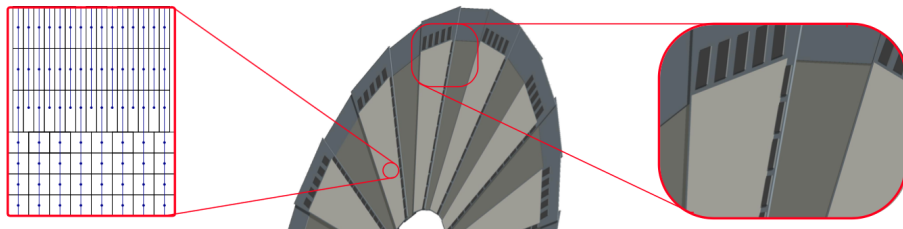


Figure 1.6: A half-disk for the FTD showing the petal concept. The rightmost zoom image shows a detail of the end-of-petal area that houses the read-out electronics. The leftmost image shows the region at $R = 8 \text{ cm}$ where both the column width and the R -dimension of the pixels changes. Figures taken from [3].

1.2.5 Electromagnetic Calorimeter

The nominal ILD detector contains a finely segmented electromagnetic sampling calorimeter (ECal). The ILD ECal has been specifically designed with particle flow calorimetry in mind. To that extent the spatial resolution of particle showers within the ECal takes as much, if not more, precedence than the energy resolution.

There are a number of design requirements for the ECal:

- The ECal must be compact in size to reduce the overall cost of the detector.
- Fine segmentation of the ECal is required so that nearby particle showers can be separated. This is an essential requirement for particle flow calorimetry.
- Electromagnetic showers should be contained within the ECal.

Based on these requirements tungsten is used as the absorber material for the ILD ECal as it has a small radiation length (X_0), a small Moli  re radius and a large ratio of radiation length to nuclear interaction length. A comparison of these properties for other ECal absorber material candidates is shown in table 1.3. The small radiation length in tungsten allows for a large number of radiation lengths, $\approx 24X_0$, to be compacted within a relatively short distance, ≈ 20 cm, in nominal ILD ECal. This is sufficient for containing all but the highest energy electromagnetic showers. The small Moli  re radius in tungsten will lead to compact electromagnetic showers. This makes separation of nearby showers easier. Finally, the large ratio of the radiation length to the nuclear interaction length in tungsten will lead to greater longitudinal separation between electromagnetic and hadronic showers again making shower identification easier.

The active material in the nominal ILD ECal is silicon, however, a scintillator strip option is also being considered. It contains a total of 30 longitudinal readout layers, which is sufficient to provide a good energy resolution. The tungsten thickness for the innermost 20 layers is 2.1 mm, while for the final 10 layers it is 4.2 mm. This configuration of absorber material thickness is chosen to reduce the number of readout channels and hence the cost, while maintaining a high sampling rate for particle showers at the start of the ECal. It should be noted that this ECal offers no gains in terms of energy resolutions in comparison to preexisting particle collider experiments, as shown in table 1.4. This is the case because the focus of this calorimeter is split between imaging the particle showers and recording their energy as opposed to purely focusing on the energy measurement. Each of the ECal layers is divided up into square cells, of side length 5 mm, which makes

separation of nearby particle showers possible. This cell size was chosen as a balance between being able to resolve nearby particle showers and reducing the overall cost of the calorimeter, which scales with the number of readout channels. An optimisation study of the various ECal parameters for the ILD detector can be found in section ??.

Material	λ_I (cm)	X_0 (cm)	ρ_M (cm)	$\frac{\lambda_I}{X_0}$
Fe	16.8	1.76	1.69	9.5
Cu	15.1	1.43	1.52	10.6
W	9.6	0.35	0.93	27.4
Pb	17.1	0.56	1.00	30.5

Table 1.3: Comparison of the nuclear interaction length λ_I , radiation length X_0 and Moliére radius for iron, copper, tungsten and lead. Table taken from [1].

Experiment	ECal Energy Resolution $\frac{\sigma_E}{E}$
CMS [5]	$\sim \frac{2.8\%}{\sqrt{E(\text{GeV})}} \oplus 0.3\% \oplus \frac{12\%}{E(\text{GeV})}$
ATLAS [6]	$\sim \frac{10.1\%}{\sqrt{E(\text{GeV})}} \oplus 0.1\%$
LHCb [7]	$\sim \frac{9\%}{\sqrt{E(\text{GeV})}} \oplus 0.8\%$
ILC (ILD Silicon Option) [3]	$\sim \frac{16.6\%}{\sqrt{E(\text{GeV})}} \oplus 1.1\%$

Table 1.4: Comparison of the ECal energy resolutions for various experiments.

1.2.6 Hadronic Calorimeter

A finely segmented hadronic sampling calorimeter (HCal) is used in the nominal ILD detector. The design requirements for the ILD HCal mirror those of the ECal, which can be found in section 1.2.5, with one exception; the HCal is designed to contain hadronic showers as opposed to electromagnetic showers. Steel is used as the absorber material for the HCal as it has durable mechanical properties that allow the HCal to be constructed without the need of auxiliary supports. If required, auxiliary supports would create dead regions in the detector that would harm performance. Furthermore, steel is relatively inexpensive and has a relatively small nuclear interaction length, meaning it is possible to achieve a compact calorimeter design at low cost. The nominal ILD HCal contains

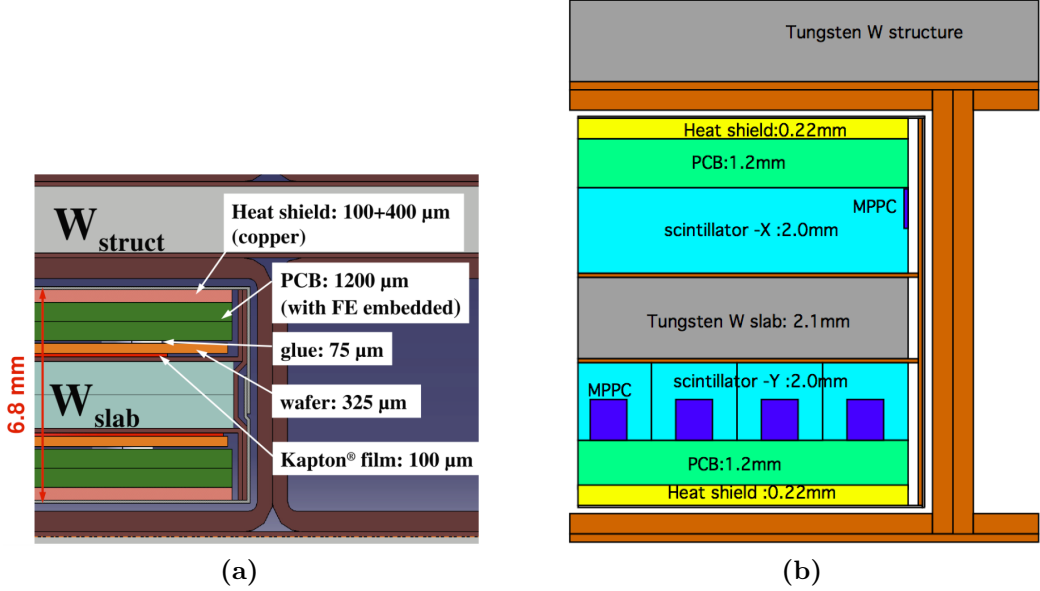


Figure 1.7: Cross section through ECal layer for (a) silicon and (b) scintillator option. Figures taken from [3].

approximately $6\lambda_I$, which when combined with the $1\lambda_I$ in the ECal is enough to contain the majority of hadronic showers at ILC like energies.

The active material in the nominal ILD HCal is scintillator. In total, the HCal contains 48 readout layers, which provides an extremely good energy resolution. This can be seen when comparing the HCal energy resolution between different experiments, as shown in table 1.5. An individual layer in the HCal is comprised of 20 mm of steel absorber material with 3 mm of scintillator active material. Each layer in the HCal is segmented into square cells, of side length 30 mm. This cell size was chosen as a balance between reducing the cost of the detector, which is proportional to the number of readout channels, and achieving the required spatial resolution to make particle flow calorimetry possible. The segmentation of the ILD HCal gives excellent spatial resolution and sufficiently good energy resolution to make the use of particle flow calorimetry a reality. An optimisation study of the various HCal parameters for the ILD detector can be found in section ??.

The ILD HCal is intrinsically non-compensating, which means that it has a different response to electromagnetic and hadronic showers. The origin of this different response is the fundamentally different mechanisms governing the propagation of electromagnetic and hadronic showers. One key difference between the mechanisms is that hadronic showers have an invisible energy component, which occurs due to effects such as neutrons

coming to rest in the detector and nuclear biding energy losses [8]. In general, this leads to a lower response from a calorimeter to a hadronic shower than an electromagnetic shower. A number of different software techniques have been developed for the linear collider experiment that attempt to correct this non-compensating response. For more details see chapter ???. The ILD ECal has a compensating response due to the use of tungsten as the absorber material [9], therefore, no additional treatment of energies is required.

Experiment	HCal Energy Resolution $\frac{\sigma_E}{E}$
CMS [10]	$\sim \frac{90\%}{\sqrt{E(\text{GeV})}} \oplus 4.8\%$
ATLAS [11]	$\sim \frac{52.1\%}{\sqrt{E(\text{GeV})}} \oplus 3.0\% \oplus \frac{1.6\%}{E(\text{GeV})}$
LHCb [7]	$\sim \frac{69\%}{\sqrt{E(\text{GeV})}} \oplus 9.0\%$
ILC (ILD Silicon Option) [3]	$\sim \frac{43.3\%}{\sqrt{E(\text{GeV})}} \oplus 1.8\%$

Table 1.5: Comparison of the HCal energy resolutions for various experiments.

1.2.7 Solenoid, Yoke and Muon System

Surrounding the ILD calorimeter system is solenoid that generates a 3.5 T magnetic field. The magnetic field produced by the coil is crucial for bending charged particles so that their momentum can be determined from the curvature of the path they transverse. Furthermore, the bending of charged particles leads to greater separation of calorimetric energy deposits between charged and neutral particles, which will reduce the effects of confusion when using particle flow calorimetry.

The magnetic field in the ILD detector is returned by an iron yoke that surrounds the solenoid. Iron is chosen for the yoke material as it has a very large permeability.

This yoke is instrumented by a muon system in the barrel and forward regions of the detector. The goal of this instrumentation is to identify muons escaping the calorimeters and to act as a tail catcher for the calorimeters. The muon system consists of 10 layers, spaced 140 mm apart, followed by 2 (3) layers spaced 600 mm apart in the barrel (endcap) region of the detector, as shown in figure 1.8. There is also an additional sensitive layer for the barrel region placed immediately outside the HCal to help with association energy deposits between the calorimeters and the yoke. As the majority of particles at ILC like

energies will be contained within the calorimeters, the energy and spatial resolution of the muon system are not critical to performance. It is for that reason that the number of layers is lower and the layer thicknesses wider in the yoke than in the calorimeters. The nominal ILD model uses 30 mm wide and 1 m long scintillator strips as the readout technology for the yoke.

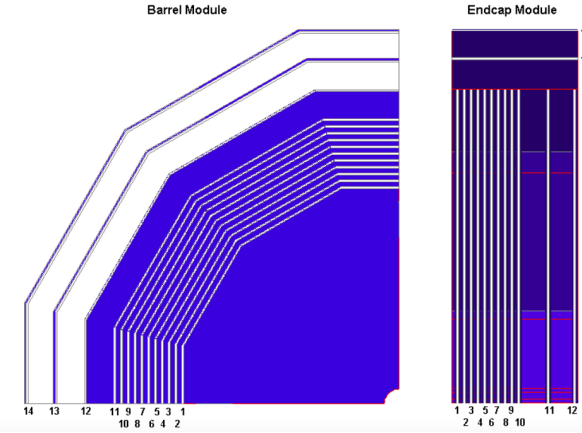


Figure 1.8: The sensitive layers of the ILD muon system. Figure taken from [3].

1.2.8 Forward Calorimetry

Forward calorimetry in the ILD detector consists of three additional sampling calorimeters:

- The LumiCal, which is located within the octagonal hole in the ECal endcap. This will give a precise measurement of the luminosity of the linear collider beam. The LumiCal uses Bhabha scattering, $e^+e^- \rightarrow e^+e^-(\gamma)$, as a gauge process for the luminosity measurement. Using this approach the luminosity can be measured with precision of less than 10^{-3} at $\sqrt{s} = 500$ GeV [4].
- The LHCAL, which is positioned within the square hole of the HCal endcap. This hadronic calorimeter is designed to extend the coverage of the HCal down to small polar angles.
- The BeamCal, which is located just in front of the final focusing quadrupole. This calorimeter will perform a bunch-by-bunch estimate of the luminosity based on the energy deposited in the calorimeter.

The layout of these calorimeters is shown in figure 1.9 and their coverage is summarised in table 1.6. Each of the forward calorimeters will have to deal with high occupancies due

to the presence of background processes, e.g. beamstrahlung, which makes fast readout crucial. Furthermore, the BeamCal experiences a large flux of low energy electrons due to its proximity to the beam pipe, which results in a large radiation dose. This makes radiation hard sensors essential for the BeamCal.

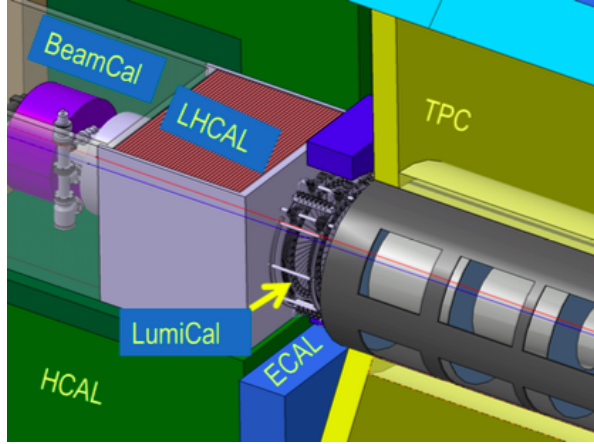


Figure 1.9: The very forward region of the ILD detector. LumiCal, BeamCal and LHCAL are carried by the support tube for the final focusing quadrupole, QD0, and the beam pipe. Figure taken from [3].

Forward Calorimeter	Polar Angle Coverage [mrad]
LumiCal	31 – 77
LHCAL	~ 29 – 122
BeamCal	5 – 40

Table 1.6: Coverage of the forward calorimeters in the ILD detector.

Each of these forward calorimeters is constructed using tungsten as the absorber material. The small Moli  re radius of tungsten ensures that narrow electromagnetic showers are formed within them, which makes separation and identification of showering particles easier.

The layout of these calorimeters is as follows:

- The LumiCal is a silicon tungsten sampling calorimeter that contains 30 readout layers. This gives the LumiCal a total depth of $\approx 24X_0$.
- The LHCAL is also a silicon tungsten sampling calorimeter, which contains 40 readout layers. The total depth of the LHCAL is $\approx 4\lambda_I$.

- The BeamCal is a tungsten based sampling calorimeter. The sensitive detector material for the BeamCal is an ongoing area of research as, due to the extremely high occupancy from the beam induced backgrounds, a very fast readout is required. The exact layer configuration of the BeamCal will depend upon the choice of sensitive detector material and hence is yet to be specified.

The segmentation within the layers, the cell size, in these forward calorimeter is yet to be fully optimised.

1.3 Simulation

Detector model simulation for all studies presented in this work was performed using MOKKA [12], a GEANT4 [13] wrapper providing detailed geometric descriptions of detector concepts for the linear collider. The MOKKA simulation of the ILD detector contains the following [3]:

- The vertex detector is simulated using silicon as the sensitive material. Support material and the cryostat are also included.
- The supplementary silicon tracking systems are included. Again, material has been added to the simulation to represent the support material for these systems. Furthermore, an estimation has been made of the material budget for power and readout cables from the vertex detector, SIT and FTD and material has been added to the simulation to represent these. The material added to represent the power and readout cables comes in the form of an aluminium cylinder running inside the TPC field cage and around a cone around the beam pipe.
- The TPC is simulated as a cylindrical volume of a gas mixture surrounded by a field cage. A conservative estimate of the endplate is included in the simulation to account for the support structure, electronics and cooling pipes for the TPC.
- As well as including the silicon tungsten sampling calorimeter, the simulation of the ILD ECal contains additional material to represent the instrumented region of the sensor and a heat shield as shown in figure 1.7.
- Simulation of the ILD HCal has a number of realistic features including detailed modelling of the electronics, detector gaps and the implementation of Birk’s law [14] for the scintillator sensitive detector elements.

- The muon system, which is the instrumentation of the iron yoke, uses scintillator as the active material in the simulation. A square cell size of side length 30 mm is assumed. This is in contrast to the nominal ILD model, but as the tail-catcher plays a minimal role in event reconstruction at ILC like energies this difference should have negligible impact.
- The forward calorimeters, the LumiCal, LHCAL and BeamCal, are all included in the simulation. Tungsten is used as the absorber material for each of the calorimeters. The LumiCal and LHCAL use a silicon readout material, while the BeamCal uses a diamond readout.

The simulation and reconstruction of the large event samples used in the studies presented in the work was performed using the ILCDIRAC [15, 16] grid production tools.

1.4 CLIC ILD

The increased collision energy of the proposed CLIC accelerator means the use of the nominal ILD detector model would be inappropriate. Therefore, a new detector model, CLIC_ILD [17, 18], based upon the nominal ILD detector model was created to cope with the experimental conditions found at the CLIC experiment. The main differences between the nominal ILD detector and CLIC_ILD are:

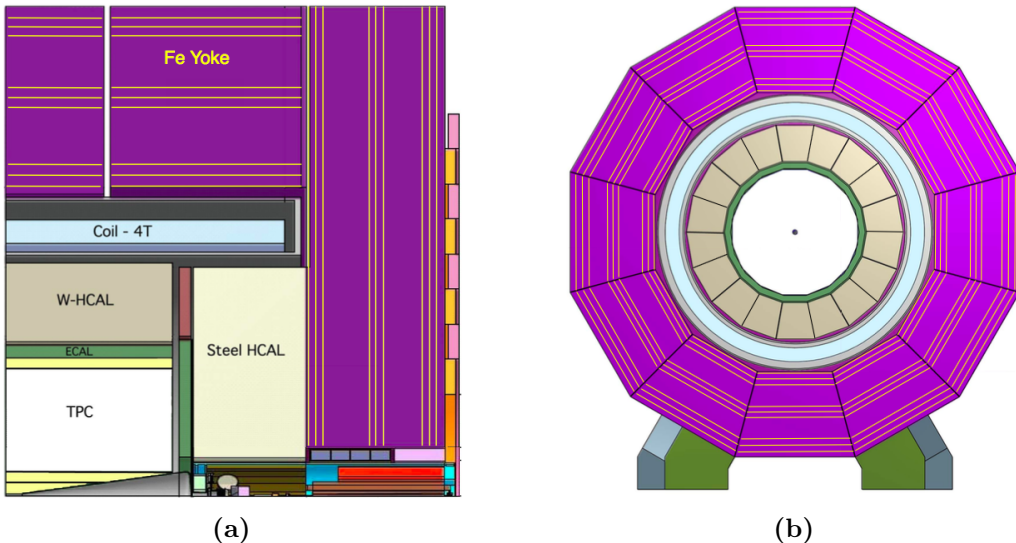


Figure 1.10: (a) Longitudinal (top quadrant) and (b) transverse cross section of the CLIC_ILD detector. Figures taken from [17].

- The higher energies found at the CLIC experiment lead to more intense beam induced backgrounds, which is especially problematic for detectors close to the IP where the occupancies will be extremely high. For this reason the inner vertex detector in CLIC_ILD is moved 15 mm further out from the IP.
- The HCal thickness is increased from $6 \lambda_I$ to $7.5 \lambda_I$. This ensures that higher energy hadronic showers found at the CLIC experiment are contained within the calorimeters.
- The HCal absorber material for the barrel is tungsten as opposed to steel. This reduces the overall thickness of the HCal and keeps the coil size, one of the driving cost factors for the detectors, similar for the nominal ILD and CLIC_ILD detectors. Steel is used as the absorber material for the HCal endcaps as there are no spatial requirements relating to the coil size and this will lower the detector cost. Furthermore, the shower development time in steel is faster than in tungsten making effective time stamping of energy deposits easier, which is crucial for the CLIC experiment for vetoing beam induced backgrounds.
- The magnetic field strength in the CLIC_ILD detector is increased to 4 T. This was found to benefit the reconstruction, particularly at high energies, as it leads to greater separation of charged particle tracks. Furthermore, it was possible to achieve this increase in field strength using the nominal ILD coil design.
- The CLIC_ILD detector contains masking, graphite layers placed in front of the BeamCal, to prevent particles produced by the beam-induced interactions from backscattering into the main detector. It is the increased collision energy that makes backscattering of particles a more problematic effect for the CLIC experiment than it is for the ILC experiment.

1.5 Particle Flow Reconstruction

Particle flow calorimetry relies upon correct associations being made between calorimetric energy deposits and charged particle tracks. Even with a finely segmented detector, such as the ILD detector described in section 1.2, correctly making these associations is a highly non-trivial task and must be done using advanced pattern recognition software. This is provided by the PandoraPFA particle flow algorithm [1, 2, 19]. PandoraPFA

is applied in the linear collider reconstruction using MARLIN [20], a c++ framework specifically designed for the linear collider.

1.5.1 PandoraPFA

PandoraPFA takes as input calorimeter hits and charged particles tracks and produces as output reconstructed particles known as particle flow objects (PFOs). The pattern recognition in PandoraPFA is applied in eight main stages [1]:

1. Track selection. The input track collections are examined to determine whether V^0 decays, two charged tracks originating from a point displaced from the IP, or kinks, where a charged particle has decayed into a single charged particle and a number of neutral ones, are present. Such information will be propagated in the reconstruction to the final PFO creation stage.
2. Calorimeter hit treatment. The treatment of calorimeter hits by PandoraPFA is of paramount importance to the work presented in chapters ?? and ???. Therefore, full details of the calorimeter hit selection procedure are presented here. This selection procedure is broken down into several steps:
 - The various collection of, post digitisation, calorimeter hits are passed into the Pandora framework and converted into Pandora calorimeter hits.
 - To minimise any dependancy on the detector geometry each calorimeter hit is assigned to a pseudo-layer, which is representative of the hits position in the calorimeter. All further topological association algorithms work using the pseudo-layer definition, illustrated in figure 1.11.
 - A minimum ionising particle equivalent energy cut is applied to the calorimeter hits. If a calorimeter hit contains less than 0.5 (0.3) of the energy of a normally incident MIP passing through the calorimeter cell in the ECal (HCal) then it is not used in the reconstruction.
 - If a calorimeter hit is sufficiently far away from other hits, it is flagged as an isolated hit. Such hits are most likely due to low energy neutrons produced in hadronic showers, which can travel a significant distance from the original shower before depositing energy. Due to the distance they travel these hits are very difficult to associate to the correct particle shower. Furthermore, as such

hits are unlikely to be the seed for a particle shower they are not used by the initial clustering algorithm.

- Any calorimeter hit that contains an energy consistent with a MIP signal and where, at most, one Pandora calorimeter hit exists in the neighbouring cells within the same layer is flagged as a MIP consistent hit. This information is used in the identification of MIPs in the reconstruction.
 - The energy contribution for each calorimeter hits ultimately depends on whether the cluster the calorimeter hit has been associated to is deemed to have originated from an electromagnetic or hadronic particle shower. Different scale factors are applied to the energy for electromagnetic and hadronic showers to account for the non-compensating response of the calorimeters. These scale factors are used throughout the reconstruction, including the final reconstructed particle energy, once the particle shower type has been identified. For energy comparisons prior to the shower type being identified the uncorrected calorimeter hit energy is used. Further details on how these calibration constants are determined can be found in chapter ??.
3. Clustering. This begins by using the projection of the charged particle tracks onto the front face of the ECal as seeds for the initial clustering phase. Calorimeter hits are looped over on a per layer basis, working from the inner to the outer pseudo-layer, and if they fall within a cone of fixed dimensions surrounding a cluster direction they are associated to the cluster. If no association can be made to any preexisting calorimeter hit clusters then the calorimeter hit is used to seed a new cluster.
 4. Topological cluster merging. The initial clustering algorithm is designed to be conservative to avoid mixing together energy deposits from several particles. The fragments produced by the initial clustering are then merged together by various algorithms whose logic is motivated by a number of well-motivated topological rules, such as those shown figure 1.12.
 5. Statistical re-clustering. Comparisons between the cluster energy and any associated track momenta are made to determine whether they are consistent. If a large discrepancy is observed then statistical re-clustering is initiated. This involves running a number of differently configured algorithms to change the cluster configuration to determine if a new optimal configuration of tracks and clusters can be found.

This step relies upon the reported cluster energies being accurate. To ensure this is the case, a well defined calibration procedure is applied for all detector models considered in this work, for more details see chapter ???. At this point in the reconstruction, the energy resolution of the calorimeters impacts the way that the pattern recognition is performed. The better the energy resolution of the calorimeters, the fewer the number of mistakes that are made when pairing up clusters of calorimeter hits to charged particle tracks.

6. Photon identification and recovery. Topological likelihood data is used to identify clusters of calorimeter hits that are consistent with γ s. This is possible due to the clear transverse and longitudinal profiles observed for electromagnetic showers.
7. Fragment removal. Neutral clusters originating from a nearby charged particle cluster are identified and merged back into the parent charged particle cluster. These algorithms take into account the changes in the compatibility of the track and cluster associations when merging any neutral clusters into charged clusters.
8. Formation of particle flow objects. Finally, reconstructed particles are produced. The energy for charged particles is taken from the track momenta, while neutral particle energies are taken from the calorimeter cluster measurements. Furthermore, the different electromagnetic and hadronic scales are applied to the output neutral particle energies depending on whether the neutral cluster is consistent with a γ .

The application of the pattern recognition algorithms in PandoraPFA when combined with a highly segmented detector make particle flow calorimetry a reality. In turn this provides excellent jet energy resolution for studying many interesting physics processes at the linear collider experiment.

1.6 Performance

The fundamental principle of particle flow calorimetry is to measure the energy of a particle passing through a detector in whichever sub-detector offers the best energy resolution. For particle collider experiments, this involves measuring the momenta of charged particles using the curvature of the track they create in the detector. This offers extremely good energy resolution in comparison to the traditional calorimetric approach.

As many physics processes of interest at the linear collider involve multi-jet final states [21], good jet energy resolution is a crucial aspect of detector performance. As

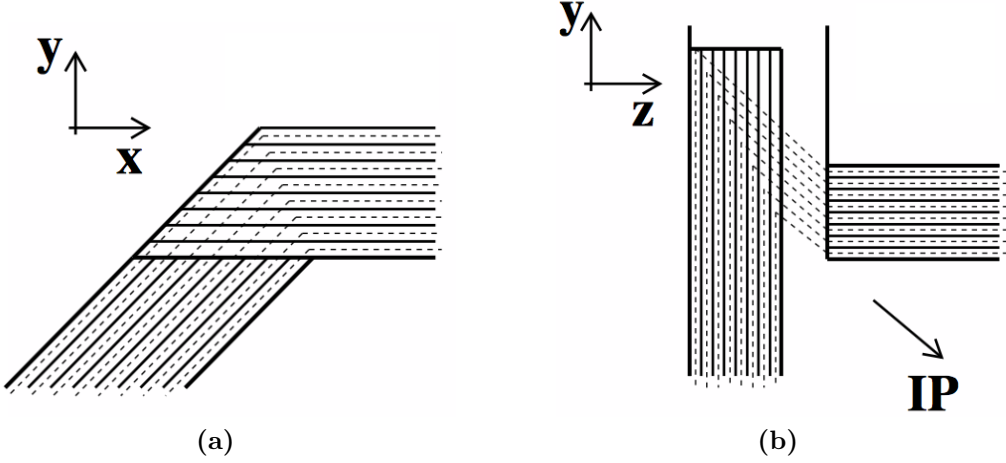


Figure 1.11: Schematic showing the definition of the pseudo-layer assignment for calorimeter hits. The solid lines indicate the positions of the physics ECal layers and the dashed lines show the definition of the virtual pseudo-layers. (a) The *xy*-view showing the ILD ECal stave structure. (b) The *xz* view showing a possible layout for the ECal barrel/endcap overlap region. The pseudo-layers are defined using projection back to the IP. Figures taken from [1].

shown in chapter 2, the sensitivity of the linear collider experiment to areas of new physics can be determined using reconstructed jet energies. Furthermore, parameters derived from the energy measurements of jets are extremely useful for identification of physics channels of interest. Therefore, a key metric for describing detector performance is the jet energy resolution. Jet energy resolution in particular can benefit from the application of particle flow calorimetry as $\approx 70\%$ of the energy of jets are carried in the form of charged particles. As particle flow aims to measure the energy of charged particles using the tracker, it has the potential to offer extremely large benefits when measuring jet energies in comparison to the traditional calorimetric approach.

1.6.1 Jet Energy Resolution

The jet energy resolution in these studies was determined through the simulation of off mass shell Z boson events decaying to light quarks (u, d, s). PYTHIA version 6.4 [22], which had been trained on fragmentation data from the OPAL experiment [23], was used to generate these events. The decay of tau leptons appearing in the day was simulated using TAUOLA [24]. Detector simulation and event reconstruction was carried out as described in sections 1.3 and 1.5 respectively.

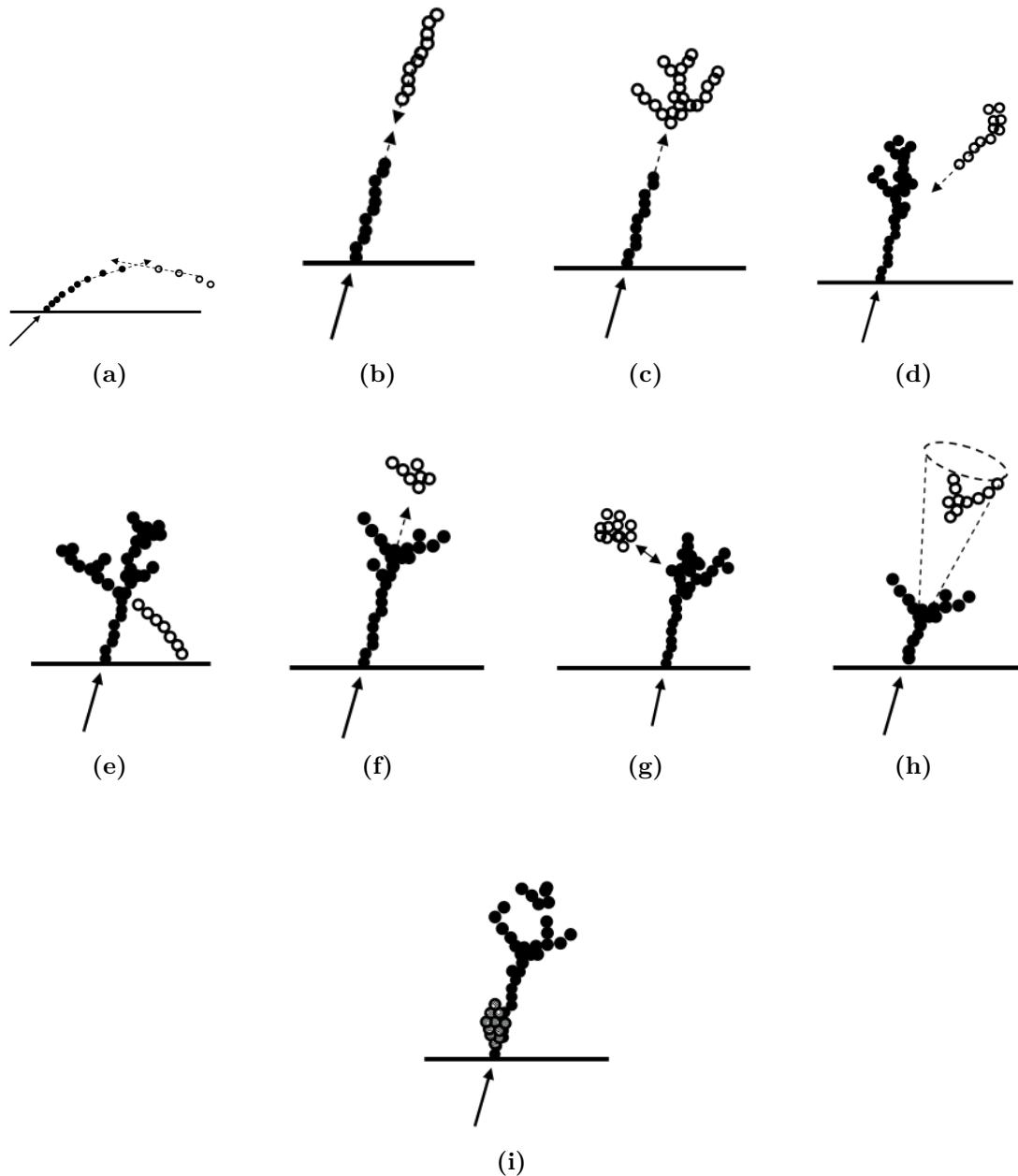


Figure 1.12: The main topological rules for cluster merging: (a) looping track segments; (b) track segments with gaps; (c) track segments pointing to hadronic showers; (d) track-like neutral clusters pointing back to a hadronic shower; (e) back-scattered tracks from hadronic showers; (f) neutral clusters which are close to a charged cluster; (g) a neutral cluster near a charged cluster; (h) cone association; and (i) recover of photons which overlap with a track segment. In each case the arrow indicates the track, the filled points represent the hits in the associated cluster and the open points represent hits in the neutral cluster. Figures taken from [1].

As the Z boson in these events is produced at rest, the typical decays form two mono-energetic jets that are produced back-to-back as shown in figure 1.13. Only events where $|\cos(\theta)| < 0.7$, where θ is the polar angle of the quarks, are used in the jet energy resolution calculation. This ensures little energy is lost down the beam axis. Using these events, the jet energy resolution was calculated as follows:

$$\frac{\text{RMS}_{90}(E_j)}{\text{Mean}_{90}(E_j)} = \frac{\text{RMS}_{90}(E_{jj})}{\text{Mean}_{90}(E_{jj})} \times \sqrt{2}, \quad (1.2)$$

where E_{jj} is the total reconstructed energy. The variables $\text{Mean}_{90}(E_{jj})$ and $\text{RMS}_{90}(E_{jj})$ are the mean and root mean squared (RMS) of the E_{jj} distribution respectively. They are calculated across the range of E_{jj} with the smallest RMS containing at least 90% of the data. This definition is used to remove the effect of outliers in the distribution [1]. If all associations between charged particle tracks and calorimeter clusters were correctly made, the reconstructed jet energy distribution would be Gaussian. However, the effect of confusion on certain events will distort this distribution and broaden the tails significantly. If the full range were to be used in the jet energy resolution calculation, the effect of these tails is overinflated. If the distribution of reconstructed jet energies is truncated to the narrowest range of the data containing at least 90% of the data, the effect of these tails can be negated. This removes events where confusion is dominant, which makes the jet energy resolution metric far more robust and representative of the bulk of the data.

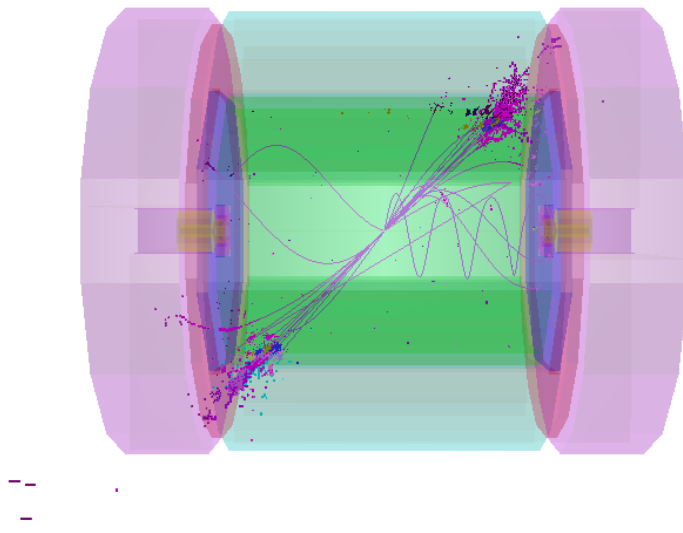


Figure 1.13: 500 GeV di-jet $Z \rightarrow u\bar{d}s$ event display for nominal ILD detector.

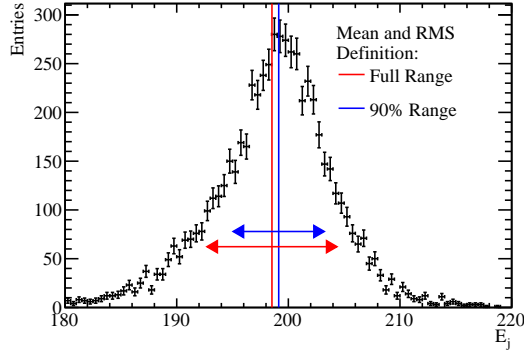


Figure 1.14: Definition of jet energy resolution. Reconstructed jet energy for 200 GeV di-jet $Z \rightarrow u\bar{d}s$ events for nominal ILD detector. The solid vertical line shows the mean of the distribution and the horizontal arrows indicate the mean \pm the root mean square (RMS) of the distribution. The red and blue lines show the mean and RMS calculated using the full range and 90% of the full range with the smallest RMS respectively.

An example of the application of this metric can be found in figure 1.14. In this example $\text{RMS}(E_j)$, the RMS calculated using the full range, is 5.8 GeV, while $\text{RMS}_{90}(E_j)$, the RMS using the reduced range, is 4.1 GeV. This corresponds to a reduction in the jet energy resolution from 4.1% to 2.9%, which clearly shows an overemphasis of the tails of the distribution when using the full jet energy range.

In the subsequent analysis a range of di-jet energies were considered ranging from the Z mass, 91 GeV, to the nominal running energy of the ILC, 500 GeV. Each event sample contained 10,000 events generated isotropically so that, given the polar angle cut, approximately 7,000 events contribute to the jet energy resolution calculation.

1.6.2 Decomposition of the Jet Energy Resolution

It is possible to gain additional insight into the detector performance by cheating the pattern recognition, the clustering of calorimeter hits together and the creation of track to cluster associations, using MC information. Cheating the pattern recognition removes the effect of confusion as it ensures no errors are made when either clustering calorimeter hits together or when associating charged particle tracks to those calorimeter clusters. This allows the detector performance to be deconstructed into two terms; one related exclusively to the intrinsic energy resolution of the detector and another related to the

pattern recognition confusion. The additional information this provides is extremely useful for characterising changes to the overall detector performance.

The intrinsic energy resolution contribution to the jet energy resolution is determined by fully cheating the pattern recognition; in this case all confusion is negated. The total confusion is defined as the quadrature difference between the jet energy resolution using the standard reconstruction and this fully cheated reconstruction. Furthermore, it is possible to cheat the pattern recognition associated with individual types of particles. This is particularly useful for studies related to the ECal as, by cheating the photon pattern recognition, it is possible to isolate the confusion associated with photons. The photon confusion is defined as the quadrature difference between the jet energy resolution using the standard reconstruction and the reconstruction where the photon pattern recognition is cheated. Examples of the calculation of the various confusion terms defined above are given in table 1.7.

Reconstruction	Jet Energy Resolution [%]
Standard Reconstruction (No MC Information)	$a = 2.97 \pm 0.05$
Cheating Entire Reconstruction	$b = 1.69 \pm 0.02$
Confusion	$\sqrt{a^2 - b^2} = 2.45 \pm 0.05$
Cheating Photon Reconstruction	$c = 2.73 \pm 0.04$
Photon Confusion	$\sqrt{a^2 - c^2} = 1.18 \pm 0.06$

Table 1.7: Example calculation of the confusion contributions to the jet energy resolution. These jet energy resolutions are for 250 GeV jets using the nominal ILD detector model and are calculated using the range of jet energies with the smallest RMS containing at least 90% of the data.

A common feature that is observed in these calibration studies is that as the intrinsic energy resolution of a calorimeter improves, the effect of confusion is reduced. This occurs as a better energy resolution means more precise comparisons can be made between the energy of a cluster of calorimeter hits and the momentum of any charged particle tracks associated to it. Comparisons such as these are made by PandoraPFA to determine whether the track cluster associations that have been made are consistent. If a large discrepancy is observed between the cluster energy and track momenta, the clustering of calorimeter hits is modified until a consistent association can be made. For more details on this comparison see chapter 1. This consistency check vastly reduces the number of errors made when clustering calorimeter hits and associating charged particle tracks to

those clusters i.e. the confusion. Therefore, improving the precision of this consistency check, by improving the energy resolution, reduces the effect of confusion.

1.6.3 Single Particle Energy Resolution

The energy resolution for individual particles is crucial for a number of physics studies of interest to the linear collider, such as γ energy resolutions in the study of anomalous triple and quartic gauge couplings [25–27]. Therefore, γ and K_L^0 energy resolutions, alongside the jet energy resolution, will be considered in these optimisation studies. As both γ and K_L^0 are uncharged, their energy measurements will be made using the calorimeters as opposed to the tracker. γ s are a natural choice of particle to consider as they are particularly relevant for several physics studies and, as they are largely contained within the ECal, they will be highly sensitive to changes in the ECal performance. K_L^0 s were used as, analogously to γ s and the ECal, their energies are primarily measured using the HCal. In general, neutral hadron energy resolutions are less crucial to physics studies, however, they do make crucial contribution to the jet energy resolution that should not be overlooked. The reported γ energy resolutions were determined using events containing a single 100 GeV γ , while the K_L^0 energy resolutions were determined using events containing a single 50 GeV K_L^0 . These energies were chosen to be as large as possible, to maximise sampling of the calorimeter response, while minimising the affect of leakage of energy from the ECal to the HCal for the γ events and leakage of energy out of the rear of the HCal for the K_L^0 events.

The energy resolution for these single particle samples is determined using a Gaussian fit to the reconstructed energy distributions. To aid convergence, the fit was applied to the narrowest range of the reconstructed energy distribution containing at least 75% of the data. The single particle energy resolution is defined as the standard deviation divided by the mean of the fitted Gaussian. For each energy resolution calculation, a total of 10,000 events were used to populate the reconstructed energy distribution. For clarity, a cut of $|\cos(\theta)| < 0.7$ was applied to veto events where particles travelled down the beam pipe or where they passed through the barrel/endcap overlap region. An example of the reconstructed energy distributions for 100 GeV γ s and 50 GeV K_L^0 s, alongside the Gaussian fits used to determine the energy resolutions, are shown in figure 1.15. The errors quoted on single particle energy resolutions are determined by propagating the errors reported from the Gaussian fit into the resolution calculation.

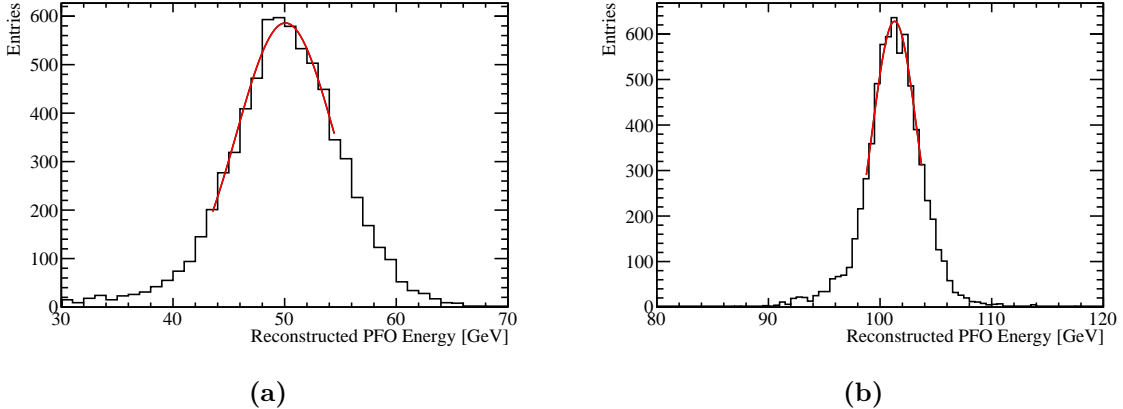


Figure 1.15: The reconstructed energy distribution for (a) 50 GeV K_L^0 and (b) 100 GeV γ events. The red line shows a Gaussian fit used to parameterise the detector performance. The fit was applied to the truncated range of the reconstructed PFO energy distribution containing at least 75% of the data with the narrowest RMS. The nominal ILD model was used in this simulation.

1.7 Summary of ILD Detector Performance

The following section outlines the nominal ILD detector performance using the metrics outlined in section 1.6.

The reconstructed energy distributions for particles whose energies are measured using calorimeters will be Gaussian. This is the case for sampling calorimeters as the active material in each calorimeter hit essentially counts the number of charged particle tracks passing through it, or possibly the number of photons for scintillator options. An estimation of the total energy deposited in a calorimeter hit, including the absorber material, can be made based upon this number of tracks or photons. For more details on how this estimation is made see chapter ???. Finally, the energy of the entire particle shower is estimated by grouping together calorimeter hits and summing their energy. As each calorimeter hit energy is an independent random measurement the particle shower energy will, by the central limit theorem, have a Gaussian distribution.

As each calorimeter hit involves counting a number of objects, charged particle tracks or photons, Poisson statistics governing the distribution of calorimeter hit energies. If the mean of the distribution of the energy of a cluster of calorimeter hits is $\lambda = N$, where N is the mean number of objects measured in the calorimeters, the standard deviation of that distribution is $\sigma = \sqrt{\lambda} = \sqrt{N}$ and the energy resolution is $\frac{\sigma}{\lambda} = \frac{1}{\sqrt{N}}$. As

the total shower energy, E_{Reco} , is proportional to N the energy resolution for a particle shower in an ideal calorimeter is $\frac{\sigma_{Reco}}{E_{Reco}} = \frac{a}{\sqrt{E_{Reco}}}$. In reality, it is typical to express the energy resolution of a calorimeter in the following form

$$\frac{\sigma_{Reco}}{E_{Reco}} = \frac{a}{\sqrt{E_{Reco}}} \oplus b \oplus \frac{c}{E_{Reco}}, \quad (1.3)$$

where the b term is a constant term that accounts for a variety of instrumental effects that do not depend on energy, e.g. mechanical imperfections, and the c term accounts for electrical noise [28]. Here \oplus denotes the quadrature sum of variables.

Prototypes of the various ILD calorimeter options have been constructed and validated using test beam measurements. The energy resolution of the ILD ECal, determined from test beam measurements, was parameterised as $\frac{16.6}{\sqrt{E_{Reco}}} \oplus 1.1\%$ for the silicon option and $\frac{12.9}{\sqrt{E_{Reco}}} \oplus 1.2\%$ for the scintillator option [3]. The electrical noise was deemed sufficiently small that the c term in the parameterisation could be neglected in both cases. These results were determined using an e^- test beam with energies ranging up to ≈ 40 GeV. This parametrisation is compared to the full ILD detector simulation in figures 1.16a and 1.16b for the silicon and scintillator ECal options respectively. The test beam parameterisation of the energy resolution for the silicon ECal option is almost identical to the energy resolution observed in the full simulation. At very high energies, ≈ 500 GeV, the ECal is no longer sufficient to fully contain the γ s and so leakage of energy into the HCal leads to a minor degradation in the simulated energy resolution. This accounts for the worse energy resolution seen in the full simulation when compared to an extrapolation of the test beam parameterisation at high energies. The test beam parameterisation of the energy resolution for the scintillator ECal option is significantly better than that observed in the full simulation, which is most likely due to an imperfect implementation of the scintillator ECal within the full detector simulation. The γ energy resolutions seen in the full ILD simulation are similar for the silicon and scintillator ECal options.

Similarly, the energy resolution, determined from test beam measurements, for the nominal ILD HCal was parameterised as $\frac{57.6}{\sqrt{E_{Reco}}} \oplus 1.6\%$ [29]. A comparison between this test beam parameterisation and the full ILD simulation, using the silicon ECal option, is shown in figure 1.16c. The test beam measurements were made using π^\pm s with energies ranging from 10 to 80 GeV, while the full ILD simulation used K_L^0 s ranging from 10 to 100 GeV. The deviation between the test beam parameterisation and the full ILD simulation, which grows as the K_L^0 energy increases, is most likely due to the treatment of energy deposits leaking out of the back of the HCal. In the test beam studies, to

minimise the effect of leakage, events were only considered if the particle showers started developing at the front of the HCal. In the full simulation studies, all particle showers were used, which means some energy will have leaked out of the back of the calorimeters and been deposited in the uninstrumented solenoid region of the detector resulting in a degradation in the energy resolution.

Figure 1.16d shows the jet energy resolution as a function of jet energy for the full ILD simulation. Alongside this, the intrinsic energy resolution and confusion contributions to the jet energy resolution are also presented. The jet energy resolution at low energies is dominated by the intrinsic energy resolution of the detector, while at high energies it is dominated by the effect of confusion. This is to be expected because the intrinsic energy resolution of the calorimeters is proportional $\frac{1}{\sqrt{E_j}}$. On the other hand, confusion grows with energy because increasing energy leads to more dense event topologies, which makes pattern recognition more challenging. The total jet energy resolution for the ILD detector are sufficiently small, $\frac{\sigma_{E_j}}{E_j} \lesssim 3.8\%$ [1, 3, 17], across the energy range considered to make separation of the hadronic decays of the W and Z bosons possible, which is one of the key requirements for the future linear collider.

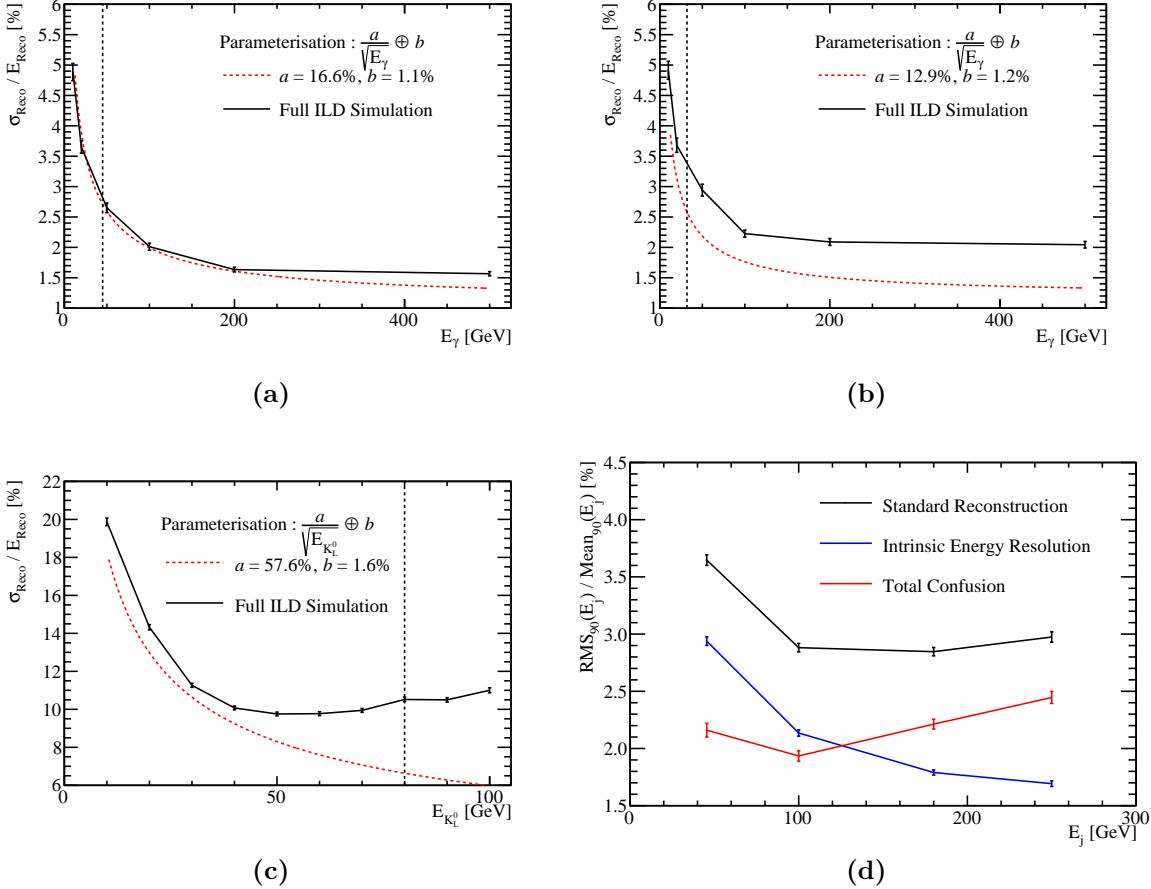


Figure 1.16: (a) The energy resolution as a function of γ energy for the silicon ECal option. The black markers indicate the energy resolutions for the full ILD simulation and the red dotted line shows the test beam parameterisation of the ECal energy resolution. (b) The energy resolution as a function of γ energy for the scintillator ECal option. The black markers indicate the energy resolutions for the full ILD simulation and the red dotted line shows the test beam parameterisation of the ECal energy resolution. (c) The energy resolution as a function of neutral hadron energy. The black markers indicate the energy resolutions for the full ILD simulation, with the silicon ECal option, which was determined using K_L^0 s. The red dotted line shows the test beam parameterisation of the HCal energy resolution, which was determined using π^\pm s. (d) The jet energy resolution (RMS_{90}) as a function of jet energy using the nominal ILD model, with the silicon ECal option. The intrinsic energy resolution and confusion contributions to these the jet energy resolutions are also presented. The black dotted vertical line on the single particle energy resolutions shows the highest energy particles used in the test beam measurements.

Chapter 2

The Sensitivity of CLIC to Anomalous Gauge Couplings through Vector Boson Scattering

“Kids, you tried your best, and you failed miserably. The lesson is, never try.”

— Homer Simpson

2.1 Motivation

Vector boson scattering is the interaction of the form $VV \rightarrow VV$ where V is any of the electroweak gauge bosons W^+ , W^- , Z or γ . This is an interesting process to study because it provides understanding of how the Standard Model Higgs is able to unitarise the otherwise unbounded cross-section for longitudinal massive gauge boson scattering. Vector boson scattering also provides insights into beyond Standard Model physics that impacts the electroweak sector by probing potential anomalous triple and quartic gauge couplings.

Triple and quartic gauge couplings lead to interactions of the form $V \rightarrow VV$ and $VV \rightarrow VV$ respectively. In the Standard Model there are five allowed vertices, shown in figure 2.1, which arise from the kinematic term $\mathcal{L}_{kin} = -\frac{1}{4}B_{\mu\nu}B^{\mu\nu} - \frac{1}{4}W_{\mu\nu}W^{\mu\nu}$ in the Standard Model Lagrangian.

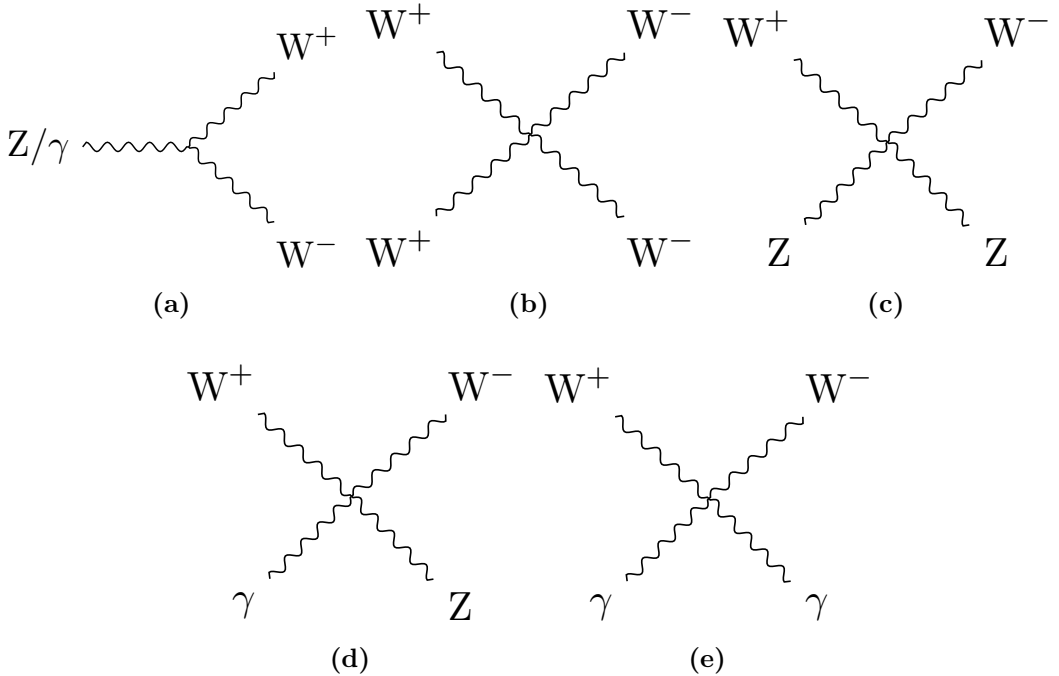


Figure 2.1: Triple and quartic gauge boson vertices in the Standard Model.

Anomalous triple and quartic gauge couplings are introduced as parameters in effective field theories (EFTs). These couplings either modify the Standard Model triple and quartic gauge boson vertices or introduce new triple and quartic vertices that were previously forbidden. EFTs are a mathematical construct designed to introduce new physics in a manner that builds upon the Standard Model. They work under the assumption that new physics exists at an energy scale, Λ , that is much higher than the energy scales currently accessible to modern day particle physics experiments. In the limit $\Lambda \rightarrow \infty$, the Standard Model is reproduced as the new physics becomes kinematically inaccessible. Such theories are model independent, giving them a wide span in the search for new physics. A classic example of an EFT theory is the Fermi theory for beta decay [30]. At energies much below the mass of the W boson, the weak interaction occurring when a neutron decays into a proton, electron and anti-neutrino can be treated as a four-point vertex with quartic coupling strength G_F , the Fermi Coupling constant as shown in figure 2.2.

The study presented in this chapter examines the anomalous quartic gauge couplings α_4 and α_5 through vector boson scattering process. The anomalous gauge couplings that are to be examined are introduced as part of an EFT that is described in chapter ???. The anomalous gauge couplings α_4 and α_5 appear in the Lagrangian through the

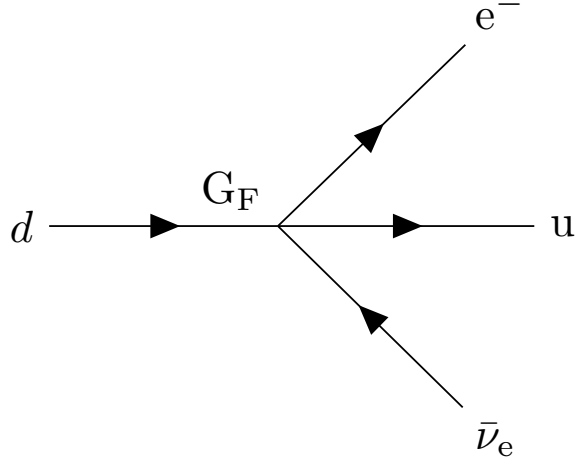


Figure 2.2: Four-point vertex proposed for explanation of beta decay by Fermi.

following terms

$$\alpha_4 [\text{Tr}(V^\mu V_\mu)]^2 \quad \text{and} \quad \alpha_5 \text{Tr}(V^\mu V_\nu) \text{Tr}(V^\nu V_\mu) , \quad (2.1)$$

where V_μ corresponds, in a carefully chosen gauge, to a linear combination of the massive gauge bosons W^+ , W^- and Z . These terms modify the Standard Model vertices $W^+W^- \rightarrow W^+W^-$ and $W^+W^- \rightarrow ZZ$ as well as introducing the new vertex $ZZ \rightarrow ZZ$. The anomalous gauge couplings α_4 and α_5 can be studied in vector boson scattering processes such as those shown in figure 2.3.

CLIC is designed for precision measurements in e^+e^- collisions at high energies and it is ideal for a study of vector boson scattering. The application of Particle Flow Calorimetry with fine granularity calorimeters gives CLIC excellent jet energy resolution, which allows it to clearly characterise multi-jet final states and final states containing missing energy in the form of neutrinos. The excellent jet energy resolution also allows for accurate separation of W and Z bosons through di-jet invariant mass, which will be invaluable for event selection.

The cross-sections for vector boson scattering processes are sufficiently large at the proposed running energies for CLIC to give large signal sample sizes. A study of anomalous gauge boson couplings at CLIC has the potential to give results several orders of magnitude better than the complementary studies performed at the LHC because of the reduction in hadronic backgrounds and increased cross-section for vector boson

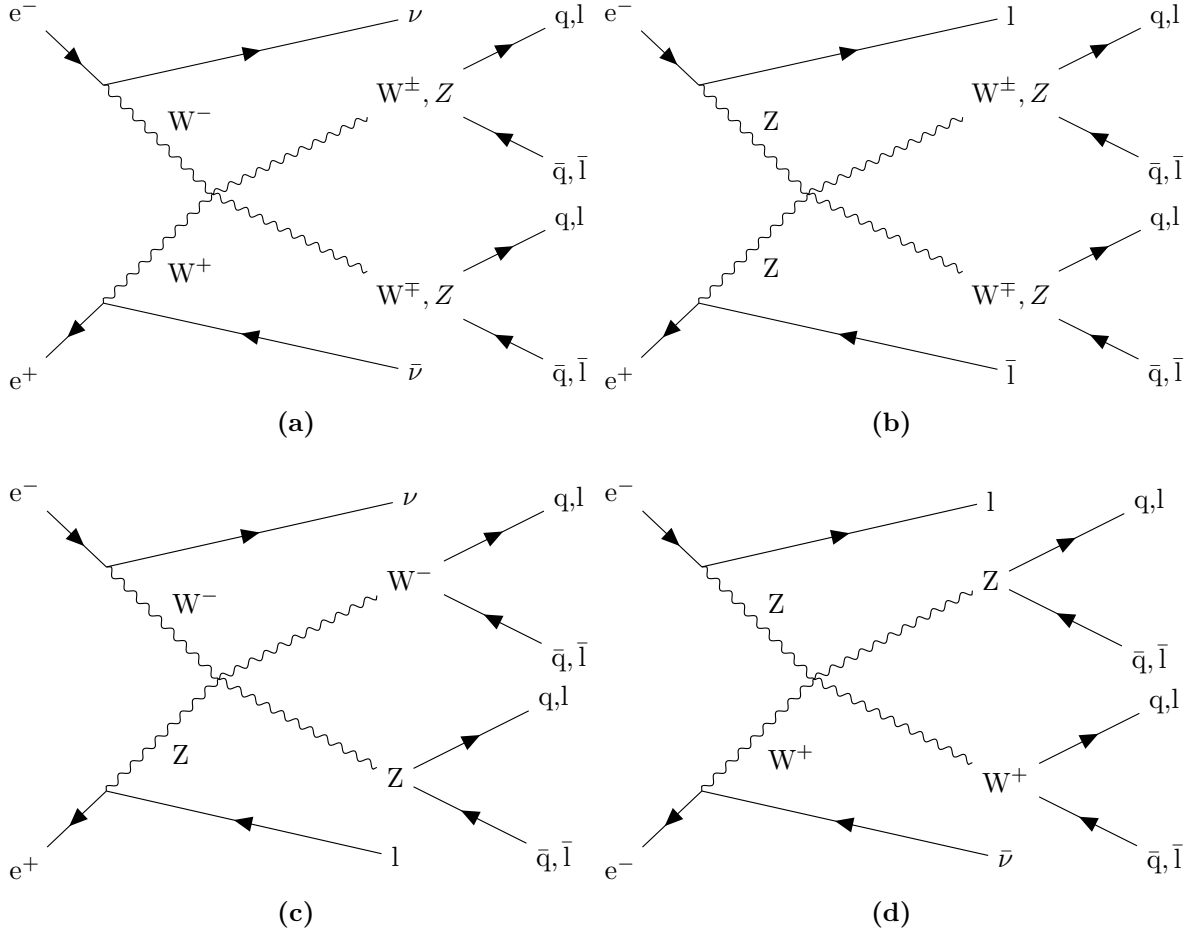


Figure 2.3: Example of vector boson scattering Feynman diagrams showing sensitivity to quartic gauge boson self-interaction vertices. The processes shown are relevant for CLIC. In these diagrams q represents the u, d, s, c and b quarks; l represents e^-, μ^- and τ^- leptons; and ν represents the ν_e, ν_μ and ν_τ neutrinos.

scattering processes [31]. The above reasons make a strong case for performing a vector boson scattering analysis at CLIC.

The branching fractions for the hadronic decays of both the W^\pm and Z bosons is of the order of 70% [32], therefore, the signal final states for the analysis presented in this chapter are vector boson scattering processes where the outgoing bosons decay purely hadronically: $\nu\nu qqqq$, $\nu lqqqq$ and $llqqqq$.

2.2 Event Generation, Simulation and Reconstruction

Events were generated using Whizard [33, 34] version 1.95. Due to the presence of beamstrahlung photons in the CLIC beam, events were generated for collisions of e^+e^- , $e^+\gamma$, γe^- and $\gamma\gamma$. The energy spectra used for all particles involved in these collisions took into account the effects of radiation in the form of beamstrahlung photons and the intrinsic energy spread of the CLIC beam. Furthermore, events involving the interaction between the electromagnetic field of the beam particles involving quasi-real photon mediators with low momenta, described by the Weizsäcker-Williams approximation [35, 36] or the Equivalent Photon Approximation (EPA), were generated using Whizard and included in this analysis. Fragmentation and hadronisation was implemented using PYTHIA 6.4 [22] that was tuned for OPAL e^+e^- collision data recorded at LEP [23]. The decays of tau leptons was simulated using TAUOLA [24]. The full list of events used in this analysis, along with their Standard Model cross-section for $\sqrt{s} = 1.4$ TeV can be found in table 2.1. The samples comprise all final states that are relevant, either as signal or background processes, for an analysis involving the purely hadronic decay channels of the vector boson scattering process:

- Final states from the purely hadronic decay channels of the vector boson scattering process. These states are expected to show sensitivity to the anomalous couplings α_4 and α_5 : $e^+e^- \rightarrow \nu\nuqqqq$, $e^+e^- \rightarrow \nu lqqqq$ and $e^+e^- \rightarrow llqqqq$
- Final states with four primary quarks arising from e^+e^- interactions: $e^+e^- \rightarrow qqqq$.
- Final states with two primary quarks arising from e^+e^- interactions: $e^+e^- \rightarrow \nu\nu qq$, $e^+e^- \rightarrow \nu lqq$, $e^+e^- \rightarrow llqq$ and $e^+e^- \rightarrow qq$.
- Final states with four primary quarks arising from the interactions of either e^+ or e^- with a beamstrahlung photon: $e^-\gamma_{BS} \rightarrow e^-qqqq$, $e^+\gamma_{BS} \rightarrow e^+qqqq$, $e^-\gamma_{BS} \rightarrow \nu_e qqqq$ and $e^+\gamma_{BS} \rightarrow \bar{\nu}_e qqqq$.
- Final states with four primary quarks arising from the interactions of either e^+ or e^- with the electromagnetic field of the opposing beam particle. These cross-sections are calculated using the EPA approximation, which represents the electromagnetic field of the opposing beam particle as a series of photons, so the final states appear as interactions of e^+ or e^- with photons: $e^-\gamma_{EPA} \rightarrow e^-qqqq$, $e^+\gamma_{EPA} \rightarrow e^+qqqq$, $e^-\gamma_{EPA} \rightarrow \nu_e qqqq$ and $e^+\gamma_{EPA} \rightarrow \bar{\nu}_e qqqq$.

- Final states with four primary quarks arising from the interaction of the electromagnetic fields of opposing beam particles using the EPA approximation: $\gamma_{\text{EPA}} \gamma_{\text{EPA}} \rightarrow \text{qqqq}$.
- Final states with four primary quarks arising from the interaction of the electromagnetic field of either e^+ or e^- using the EPA approximation with a beamstrahlung photon: $\gamma_{\text{EPA}} \gamma_{\text{BS}} \rightarrow \text{qqqq}$ or $\gamma_{\text{BS}} \gamma_{\text{EPA}} \rightarrow \text{qqqq}$.
- Final states with four primary quarks arising from the interaction of two beamstrahlung photons: $\gamma_{\text{BS}} \gamma_{\text{BS}} \rightarrow \text{qqqq}$.

In the above list q represents u, \bar{u} , d, \bar{d} , s, \bar{s} , c, \bar{c} , b or \bar{b} ; l represents e^\pm , μ^\pm or τ^\pm ; and ν represents ν_e , $\bar{\nu}_e$, ν_μ , $\bar{\nu}_\mu$, ν_τ and $\bar{\nu}_\tau$.

Monte-Carlo (MC) samples were simulated using the CLID_ILD detector model [4]. Further details of this detector model can be found in chapter 1. The simulation was performed in MOKKA [12], which is a GEANT4 [13] wrapper providing detailed geometric descriptions of detector concepts for the linear collider. Events were reconstructed using the MARLIN [20] c++ framework, designed for reconstruction at the linear collider. PandoraPFA [1, 2] was used to apply Particle Flow Calorimetry in the reconstruction, the full details of which can be found in chapter 1.

The effect of the $\gamma\gamma \rightarrow \text{hadrons}$ backgrounds, discussed in section ??, were incorporated in the analysis by overlaying $\gamma\gamma \rightarrow \text{hadrons}$ events onto the signal and background event samples. The overlaid backgrounds were added prior to reconstruction so that their impact on the reconstruction was fully accounted for. For each physics event of interest, $\gamma\gamma \rightarrow \text{hadrons}$ background events equivalent to 60 bunch crossings (BXs) are included. As readout time windows are applied in detector readout, 60 BXs is sufficient for accounting for the $\gamma\gamma \rightarrow \text{hadrons}$ backgrounds. These backgrounds occur in a time window of -5 ns to 25 ns around the physics event and the BXs are separated by 0.5 ns, to mimic the CLIC bunch train structure. The number of background events overlaid per BX is drawn from a Poisson distribution with a mean of 1.3 (3.2) events per bunch crossing at $\sqrt{s} = 1.4$ (3) TeV [17].

Detector readout is simulated using a readout time window, of 10 ns on all detectors apart from the TPC and HCal barrel. In the TPC, all hits are retained and in the HCal barrel a 100 ns time window is used to account for the additional time it takes hadronic showers to develop in tungsten [17]. All readout times are corrected for straight

Final State	Cross Section [fb]
$e^+e^- \rightarrow \nu\nuqqqq$	24.7
$e^+e^- \rightarrow \nu lqqqq$	110.4
$e^+e^- \rightarrow llqqqq$	62.1
$e^+e^- \rightarrow qqqq$	1245.1
$e^+e^- \rightarrow \nu\nu qq$	787.7
$e^+e^- \rightarrow \nu lqq$	4309.7
$e^+e^- \rightarrow llqq$	2725.8
$e^+e^- \rightarrow qq$	4009.5
$e^- \gamma_{\text{EPA}} \rightarrow e^- qqqq$	287.1
$e^- \gamma_{\text{BS}} \rightarrow e^- qqqq$	1160.7
$e^+ \gamma_{\text{EPA}} \rightarrow e^+ qqqq$	286.9
$e^+ \gamma_{\text{BS}} \rightarrow e^+ qqqq$	1156.3
$e^- \gamma_{\text{EPA}} \rightarrow \nu_e qqqq$	32.6
$e^- \gamma_{\text{BS}} \rightarrow \nu_e qqqq$	136.9
$e^+ \gamma_{\text{EPA}} \rightarrow \bar{\nu}_e qqqq$	32.6
$e^+ \gamma_{\text{BS}} \rightarrow \bar{\nu}_e qqqq$	136.4
$\gamma_{\text{EPA}} \gamma_{\text{EPA}} \rightarrow qqqq$	753.0
$\gamma_{\text{EPA}} \gamma_{\text{BS}} \rightarrow qqqq$	4034.8
$\gamma_{\text{BS}} \gamma_{\text{EPA}} \rightarrow qqqq$	4018.7
$\gamma_{\text{BS}} \gamma_{\text{BS}} \rightarrow qqqq$	21406.2

Table 2.1: Cross sections of signal and background processes for $\sqrt{s} = 1.4$ TeV. In the above table q represents u, \bar{u} , d, \bar{d} , s, \bar{s} , c, \bar{c} , b or \bar{b} ; l represents e^\pm , μ^\pm or τ^\pm ; and ν represents ν_e , $\bar{\nu}_e$, ν_μ , $\bar{\nu}_\mu$, ν_τ and $\bar{\nu}_\tau$. The EPA and BS subscript on the incoming photon indicates whether the photon is generated from the equivalent photon approximation or beamstrahlung.

time-of-flight to the impact point (IP). Any hits that have are measured outside of these windows are not used in the reconstruction.

2.3 Modelling of Anomalous Gauge Couplings

The samples that were sensitive to the anomalous gauge couplings α_4 and α_5 were generated using Whizard version 1.97, instead of the previously quoted version 1.95. This change was required as version 1.97 contained a unitarisation scheme that ensured

cross-sections for processes involving longitudinal gauge boson scattering did not violate unitarity at the energies considered here.

Two alternative methods exist for modelling the sensitivity of the vector boson scattering process to the anomalous gauge couplings α_4 and α_5 . The first is to generate multiple samples with different values of α_4 and α_5 and the second is to generate a single sample with $\alpha_4 = 0$ and $\alpha_5 = 0$ and reweight that sample. The latter approach was taken in this analysis as the former approach is impractical when considering a fine sampling of the α_4 and α_5 space.

Event weights, w , are calculated according to the ratio of the matrix elements, M , for the particular event configuration [37]

$$w(\alpha_4, \alpha_5) = \frac{|M(\text{event}, \alpha_4, \alpha_5)|^2}{|M(\text{event}, 0, 0)|^2}. \quad (2.2)$$

Figure 2.4 shows the dependence of the event weights on α_4 and α_5 for four individual $\nu\nu\text{qqqq}$ final state events, generated for $\sqrt{s} = 1.4$ TeV.

Only final states involving contributions from massive gauge boson quartic vertices require reweighting. Whizard was used to evaluate the cross-sections for all final states shown in table 2.1 with $\alpha_4 = \alpha_5 = 0$ and with $\alpha_4 = \alpha_5 = 0.05$. Only the three final states shown in table 2.2 were found to have a dependency on α_4 and α_5 .

Final State	Cross Section [fb] ($\alpha_4 = \alpha_5 = 0.00$)	Cross Section [fb] ($\alpha_4 = \alpha_5 = 0.05$)	Percentage Change[%]
$e^+e^- \rightarrow \nu\nu\text{qqqq}$	24.7	34.6	+40.1
$e^+e^- \rightarrow \nu\text{lqqqq}$	115.3	113.0	-2.0
$e^+e^- \rightarrow \text{llqqqq}$	62.1	68.6	+10.5

Table 2.2: Cross sections for selected processes showing the effect of the anomalous gauge couplings α_4 and α_5 for $\sqrt{s} = 1.4$ TeV.

To maximise the sensitivity to the anomalous gauge couplings, the $\nu\nu\text{qqqq}$ final state is used to define signal in this analysis. The νlqqqq and llqqqq final states are treated as backgrounds that are invariant to changes in α_4 and α_5 because they have a much reduced sensitivity to the anomalous gauge couplings in comparison to the $\nu\nu\text{qqqq}$ final state. Furthermore, the νlqqqq and llqqqq final states can be easily vetoed during event selection because of the presence of the primary lepton. This means the sensitivity of the

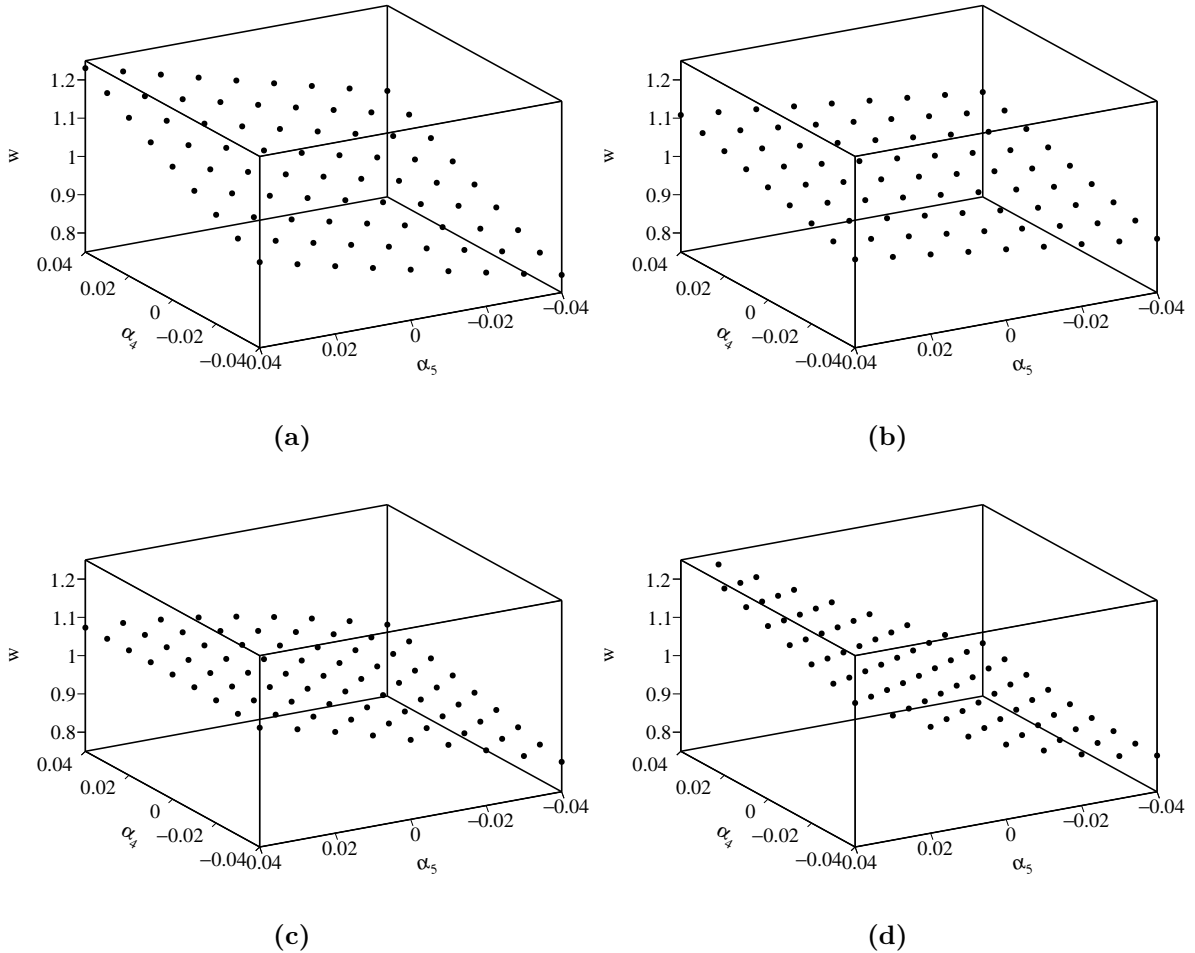


Figure 2.4: The event weights, w , determined by the generator as a function of the anomalous couplings α_4 and α_5 for a selection of $\nu\nu\text{qqqq}$ final state events for $\sqrt{s} = 1.4$ TeV.

νlqqqq and llqqqq final states to the anomalous gauge couplings will have a negligible effect on the results from this study.

Use of the unitarisation scheme in Whizard 1.97, which is needed to ensure cross-sections do not violate unitarity when studying anomalous gauge couplings at CLIC like energies, requires a unit CKM matrix [37]. The impact of this requirement was examined by comparing several reconstructed and MC distributions for $\nu\nu\text{qqqq}$ final state events generated with Whizard using a Standard Model and unit CKM matrix. No significant differences were observed, which indicates that enforcing a unit CKM matrix when generating the $\nu\nu\text{qqqq}$ final state samples did not significantly affect this analysis.

2.4 Data Analysis

The following section contains a description of how the variables used throughout the anomalous gauge coupling sensitivity study were determined.

2.4.1 Limiting Beam Related Backgrounds

During the reconstruction, after the inner detector tracks have been reconstructed, the CLICTrackSelection processor [2] is applied, which vetoes poorly reconstructed and fake tracks by applying simple quality cuts to the number of hits in the tracking sub-detectors. The CLICTrackSelection processors also reject tracks where the time of arrival at the calorimeter differs by more than 50 ns between a straight line of flight and a helix fit to the track. Applying this cut ensures that associations made between charged particles tracks and calorimetric energy deposits are consistent.

Following the reconstruction, the CLICPfoSelector processor [2] is applied to remove reconstructed particle flow objects (PFOs) that originate from beam related backgrounds. This processor applies cuts on the p_T and timing information of the PFOs, which vary as a function of position in the detector and the PFO type to target regions of the detector where backgrounds are more prominent, e.g. low p_T for $\gamma\gamma \rightarrow hadrons$ events. Three configurations of the CLICPfoSelector have been developed for the CLIC environment and were considered in this analysis. They are, in order of increasing background rejection, the Loose, Default and Tight selections [2].

2.4.2 Jet Finding

After the application of the CLICPfoSelector, the MarlinFastJet processor, a wrapper for the FastJet [38] processor, was used to cluster each event into four jets. These jets are then paired up to form two candidate bosons working under the assumption that the correct pairing is achieved when the difference between the invariant masses of the candidate bosons is a minima. In the case of the signal final state, $\nu\nu qqqq$, it is assumed that the four jets and two candidate bosons map onto the four primary quarks and two outgoing bosons in the vector boson scattering process. The jet clustering was performed using the longitudinally invariant k_t jet algorithm [39, 40] in exclusive mode. The longitudinally invariant k_t algorithm proceeds as follows

- Determine the k_t distance, d_{ij} , for each pair of particles, i and j , and the beam, d_{iB} , distance for each particle, i . These distances are defined as

$$d_{ij} = \min(p_{ti}^2, p_{tj}^2) \Delta R_{ij}^2 / R^2 , \quad (2.3)$$

$$d_{iB} = p_{ti}^2 , \quad (2.4)$$

where $\Delta R_{ij}^2 = (y_i - y_j)^2 + (\phi_i - \phi_j)^2$, p_{ti} is the transverse momentum of particle i , y_i is the rapidity of particle i , ϕ_i is the azimuthal angle of the direction of travel of particle i and R is a configurable parameter that typically is of the order of 1.

- Find the minimum distance, d_{\min} , of all the k_t and beam distances. If the minimum occurs for a k_t distance, particles i and j are merged, summing their 4-momenta. If the beam distance is the minima, particle i was declared to be part of the "beam" jet and the particle is removed from the list of particles and not included in the final jet output.
- Repeat until the desired number of jets is created. Alternatively, in inclusive mode this would be repeated until no particles are left in the event.

Two other clustering algorithms were considered, however, they were found to be inappropriate for the experimental conditions at CLIC. These alternative algorithm choices are applied in the same manner as the longitudinally invariant k_t algorithm, however, they differ in the definition of d_{ij} and d_{iB} . Figure 2.5 shows the distribution of the invariant mass of the candidate bosons for $\sqrt{s} = 1.4$ TeV $\nu\nu qqqq$ final state events for each of the jet algorithms considered. The candidate boson masses are determined by forcing the events into 4 jets and then pairing the jet pairs to form candidate bosons. The jet pairing configuration is determined by pairing jets such that the mass differences between the two candidate bosons is a minimum.

The first alternative jet algorithm considered was the k_t algorithm for e^+e^- colliders [41], the $e^+e^-k_t$ or Durham algorithm. In this algorithm d_{iB} is not used and

$$d_{ij} = 2\min(E_i^2, E_j^2)(1 - \cos\theta_{ij}) , \quad (2.5)$$

where θ_{ij} is the opening angle of particles i and j and E_i is the energy of particle i . In the collinear limit d_{ij} corresponds to the relative transverse momenta of the particles. The major failure of this algorithm when applied to CLIC is the absence of d_{iB} , which leads to large numbers of beam related background particles being associated to jets. As figure 2.5 shows, the invariant mass of the paired jets, which should peak around

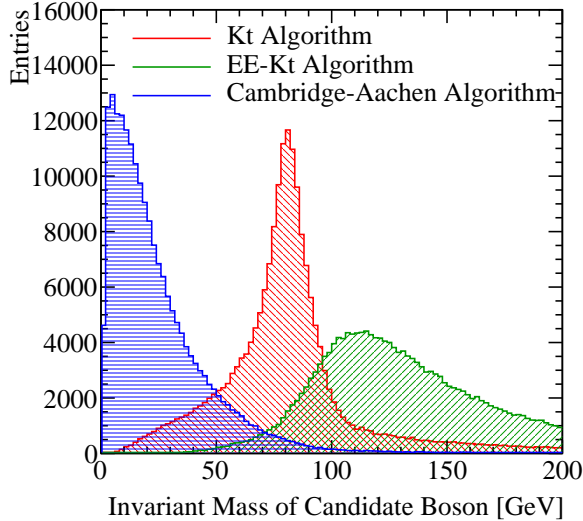


Figure 2.5: The reconstructed masses for different choices of jet algorithm for $\sqrt{s} = 1.4$ TeV $\nu\nu qqqq$ final state events. These samples should be dominated by vector boson scattering involving pairs of outgoing W bosons and so it is expected that a peak at the W boson mass, $m_W = 80.385 \pm 0.015$ GeV [32], should be observed. In the case of the k_t algorithm and the $e^+e^- k_t$ algorithm an R parameter of 0.7 was used. All distributions show raw number of events.

the W and Z boson masses, is much larger than expected, due to the presence of these backgrounds. Also this algorithm is not invariant to boosts along the beam direction meaning that it is inappropriate for use at CLIC given the beam induced backgrounds modify the nominal collision kinematics.

The second alternative jet algorithm considered was the Cambridge-Aachen jet algorithm [42] where

$$d_{ij} = \Delta R_{ij}^2 / R^2 , \quad (2.6)$$

$$d_{iB} = 1 . \quad (2.7)$$

This algorithm performs poorly as it does not account for the transverse momentum or the energy of the particles being clustered. In essence, this is a cone clustering algorithm with a cone radius defined through $\Delta R_{ij} = R$, which even for large R was found to discard too much energy in the event to be useful for this analysis. This can be seen in figure 2.5 where the invariant mass of the paired jets is much lower than expected. This algorithm is appropriate for events that contain highly boosted jets, however, at CLIC the jets are too disperse for this algorithm to be successful.

2.4.2.1 Optimal Jet Finding Algorithm

Optimisation of the jet finding procedure was performed on both the PFO selection and the value of the R parameter used in the longitudinally invariant k_t algorithm. The optimisation procedure involved performing the sensitivity study, described in section 2.6, using solely the $\nu\nu\text{qqqq}$ signal final state. This methodology ensures that the optimisation was done with respect to the physics of interest without having to perform the jet reconstruction for the large number of background events for each jet algorithm configuration considered.

Table 2.3 shows the one σ confidence limits on the measurement of α_4 and α_5 obtained using the $\nu\nu\text{qqqq}$ signal final state only at $\sqrt{s} = 1.4$ TeV for different jet algorithm configurations. These confidence limits represent the idealised sensitivity of the CLIC experiment to the anomalous gauge couplings. Once the effects of backgrounds and event selection are included in the analysis, these confidence limits will increase in size.

R Parameter	PFO Selection		
	Tight Selected PFOs	Selected PFOs	Loose Selected PFOs
0.7	$-0.0039 < \alpha_4 < 0.0051$	$-0.0035 < \alpha_4 < 0.0047$	$-0.0037 < \alpha_4 < 0.0047$
	$-0.0027 < \alpha_5 < 0.0031$	$-0.0025 < \alpha_5 < 0.0031$	$-0.0024 < \alpha_5 < 0.0028$
0.9	$-0.0036 < \alpha_4 < 0.0047$	$-0.0035 < \alpha_4 < 0.0045$	$-0.0035 < \alpha_4 < 0.0045$
	$-0.0026 < \alpha_5 < 0.0031$	$-0.0023 < \alpha_5 < 0.0027$	$-0.0022 < \alpha_5 < 0.0027$
1.1	$-0.0036 < \alpha_4 < 0.0047$	$-0.0036 < \alpha_4 < 0.0048$	$-0.0036 < \alpha_4 < 0.0046$
	$-0.0026 < \alpha_5 < 0.0031$	$-0.0025 < \alpha_5 < 0.0029$	$-0.0024 < \alpha_5 < 0.0028$

Table 2.3: One σ confidence limits on the measurement of α_4 and α_5 obtained using the $\nu\nu\text{qqqq}$ signal final state only at $\sqrt{s} = 1.4$ TeV for different jet algorithm configurations.

The configuration for the jet algorithm for the $\sqrt{s} = 1.4$ TeV analysis was chosen as selected PFOs with an R parameter of 0.9. While the loose PFO selection gives a marginally better performance, the selected PFO selection was preferred to minimise the effects of the $\gamma\gamma \rightarrow \text{hadrons}$ background. Figure 2.6a shows confidence contours, given a null hypothesis of $\alpha_4 = \alpha_5 = 0$, for the selected PFO and R parameter of 0.9 jet algorithm configuration for $\sqrt{s} = 1.4$ TeV. Figures 2.6b and 2.6c show the one dimensional χ^2 distribution for α_4 and α_5 , assuming $\alpha_5 = 0$ and $\alpha_4 = 0$ respectively, for the same configuration.

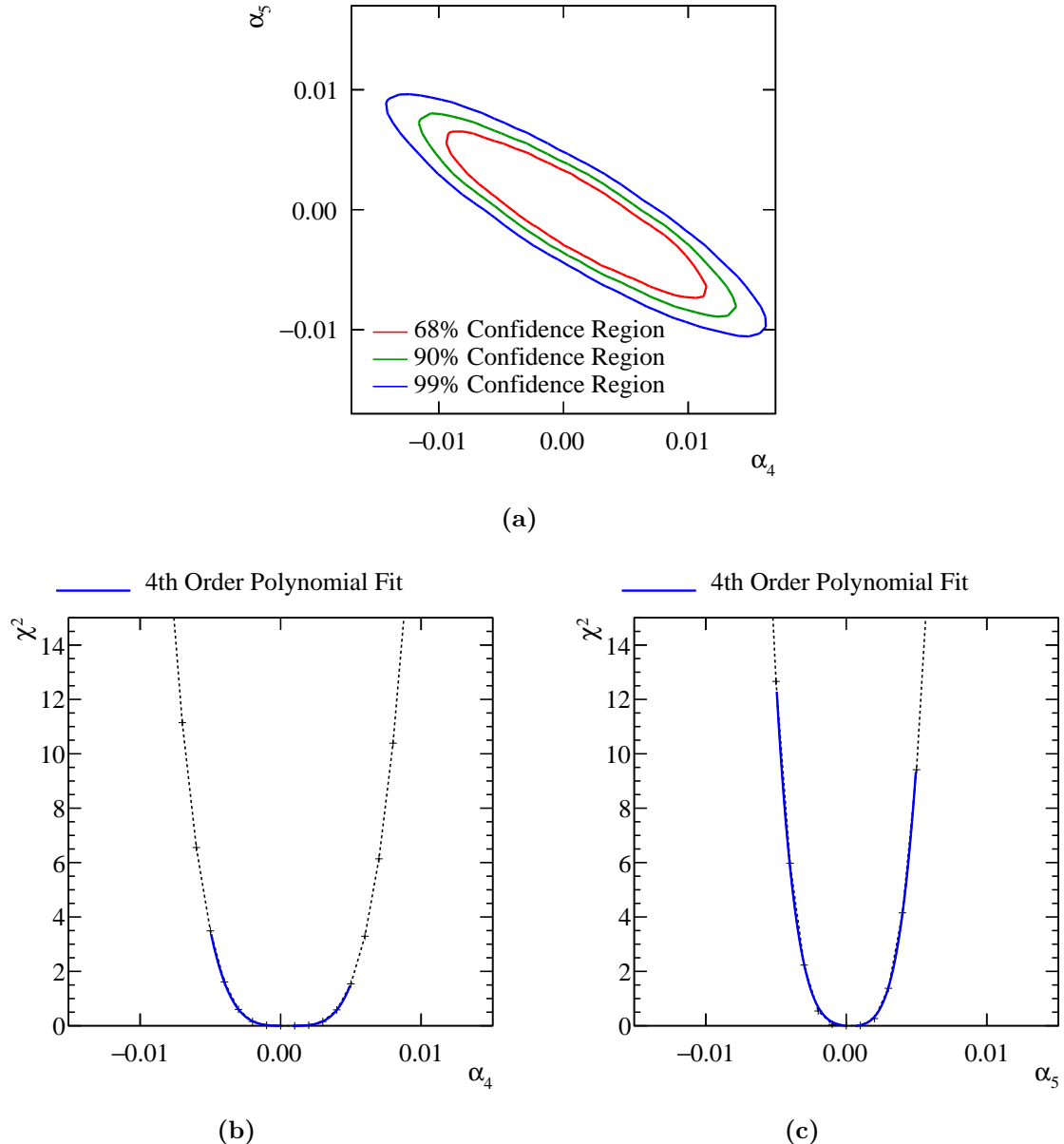


Figure 2.6: χ^2 sensitivity distributions from a fit to M_{VV} for the signal $qqqq\nu\nu$ final state only for $\sqrt{s} = 1.4$ TeV. These results use the optimal jet algorithm configuration of selected PFOs and an R parameter of 0.9 in the k_t algorithm. (a) χ^2 sensitivity contours in α_4 and α_5 space. (b) χ^2 as a function of α_4 assuming $\alpha_5 = 0$. (c) χ^2 as a function of α_5 assuming $\alpha_4 = 0$. All distributions are normalised to an integrated luminosity of $\mathcal{L}_{int} = 1.5 \text{ ab}^{-1}$.

2.4.3 Lepton Finding

An isolated lepton finder [43] was included in the analysis chain to reject background final states containing primary leptons. Leptons produced via hadronisation are unlikely to be flagged as isolated because all hadronisation products are boosted along the direction of the parent quark. This means isolated leptons are likely to correspond to primary leptons, which makes the number of isolated leptons a powerful discriminating variable to use in event selection.

The isolated lepton finder determines whether a PFO is an electron or muon by first checking that the PFO has a single charged particle track associated to it. If that is the case, the calorimetric energy deposits of the PFO are examined to see if they are consistent with what is expected for an electron or muon. If they are consistent with expectations, the properties of the charged particle track are examined to determine whether the track originates from the IP. If the PFO is deemed to have originated from the IP, isolation checks, which examine the energy deposited in the calorimeters within a cone surrounding the PFO, are applied to determine whether the particles belongs to a jet. If the PFO does not appear to belong to a jet then it is counted as an isolated lepton. The fraction of events rejected by the lepton finder is summarised in table 2.4.

Final State	$\epsilon_{\text{Lepton Finding}}$
$e^+e^- \rightarrow \nu\nu qqqq$	99.7
$e^+e^- \rightarrow \nu lqqqq$	48.9

Table 2.4: The fraction of events rejected by of isolated lepton finding for $\sqrt{s} = 1.4$ TeV for the $\nu\nu qqqq$ and $\nu lqqqq$ final states.

2.4.4 Discriminant Variables

The next stage of the analysis involved the calculation of a number of event-based variables that were found to be useful for this analysis. The variables that were calculated are as follows

- Particle level variables:
 - Number of PFOs in each jet;
 - Energy of the highest energy PFO;

- Energy of the highest energy electron;
- Cosine of the polar angle of the highest energy track;
- The number of isolated leptons found using the isolated lepton finder.

• **Candidate boson** variables:

- Energy of the candidate bosons;
- Invariant mass of the candidate bosons;
- Acolinearity of the candidate boson pair, which is defined as 180 degrees minus the opening angle of the pair of bosons in the rest frame of the detector.

• **Event based** variables:

- The invariant mass of the visible system, M_{VV} ;
- The vector sum of the transverse momentum of all PFOs in the event;
- Sphericity, defined through the sphericity tensor S^{ab} ;

$$S^{ab} = \frac{\sum_i p_i^\alpha p_j^\alpha}{\sum_{i,\alpha=1,2,3} |p_i^\alpha|^2} \quad (2.8)$$

Where p_i are the components of the momenta of PFO i in the rest frame of the detector and the sum Σ_i runs over all particles in the event. Sphericity is defined as $S = \frac{3}{2}(\lambda_2 + \lambda_3)$, where λ_i are the eigenvalues of the sphericity tensor defined such $\lambda_1 \geq \lambda_2 \geq \lambda_3$. This provides a measure of how spherical the reconstructed event topology is with isotropic events having $S \approx 1$, while two jet events have $S \approx 0$.

• **Jet clustering parameters** variables:

- The y_{ij} variables where $i = 3, 4$ and $j = i + 1$. These are the smallest k_t distance found when combining j jets into i jets.

2.4.5 Jet Energy Resolution at CLIC

The importance of the jet energy resolution, which is extensively discussed in chapters ?? and ??, should be emphasised at this point. Many of the discriminant variables that are calculated for this analysis are dependant upon the jet energy resolution. In particular,

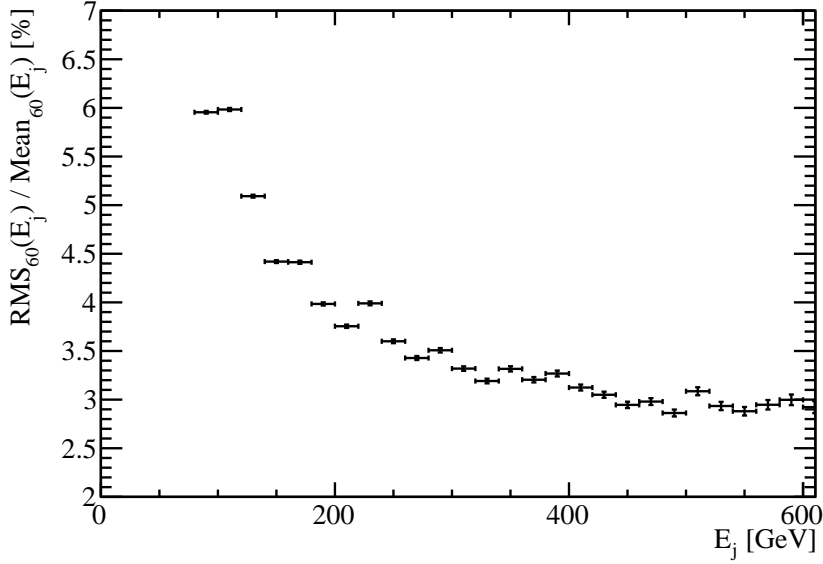


Figure 2.7: The jet energy resolution as a function of the jet energy for the $\nu\nu\text{qqqq}$ final state for $\sqrt{s} = 1.4$ TeV.

all variables related to the candidate bosons that are formed from pairing up jets, are dependent upon the measurement of jet energies.

Figure 2.7 shows the jet energy resolution as a function of the MC jet energy for the $\nu\nu\text{qqqq}$ event sample used in the $\sqrt{s} = 1.4$ TeV analysis. The MC jet energy was obtained by pairing up quarks appearing in the final state to the reconstructed jets. The events were then binned in terms of their MC jet energy and the jet energy resolution calculated for each bin. When calculating the jet energy resolution, a narrower range of jet energies was used in compared to previous studies, 60% of the data with narrowest RMS as opposed to 90%, to minimise the effects of jet finding and beam-induced backgrounds. The jet energy resolutions reported here are worse than those quoted in earlier chapters. This is to be expected given the effects of jet finding and beam-induced backgrounds.

2.5 Event Selection

This section discusses the event selection procedure. The goal of this procedure is to isolate the $\nu\nu\text{qqqq}$ final state from the background final states, i.e. those containing two and four primary quarks. The procedure consists of a set of preselection cuts followed by the application of a multivariate analysis (MVA). All event numbers have

been normalised, prior to event selection, to an integrated luminosity of $\mathcal{L}_{int} = 1.5 \text{ ab}^{-1}$ for the $\sqrt{s} = 1.4 \text{ TeV}$ analysis and $\mathcal{L}_{int} = 2 \text{ ab}^{-1}$ for the $\sqrt{s} = 3 \text{ TeV}$ analysis.

2.5.1 Preselection

A refined selection of the $\nu\nu\text{qqqq}$ signal final state is achieved using a MVA, however, to ensure efficiency in the training and application of that MVA a number of simple preselection cuts were developed to veto obvious background final states prior to the application of the MVA. Preselection cuts were applied to the transverse momentum of the system and the number of isolated leptons found in the event. The raw distributions of these variables is shown in figure 2.8 and based on these distributions the following cuts were applied

- Transverse momentum of system $> 100 \text{ GeV}$. This cut is effective due to the presence of missing energy in the form of neutrinos in the signal final state.
- Number of isolated leptons in system $= 0$. This cut is effective as the signal final state does not contain leptons, while numerous background final states do.

The impact of these preselection cuts can be found in table 2.5, which can be found on page 56.

2.5.2 Multivariate analysis

Having established the preselection cuts, a MVA was applied using the TMVA toolkit [44], to refine the event selection. The signal and background final state samples were separated into two equally sized samples; one sample was used to independently train the MVA and the other sample was used in the subsequent analysis.

The performance of several MVA classifiers was examined to determine the optimal classifier for this analysis. The MVA classifiers considered were [44]:

- **Boosted Decision Tree (BDT).** Decision trees are formed by the sequential application of cuts that split the data into multiple classes. After the application of the final cut, the remaining classes are used to classify whether the input event corresponds to signal or background. Boosting a decision tree involves the use of several decision trees. A single classifier output is obtained from a weighted average

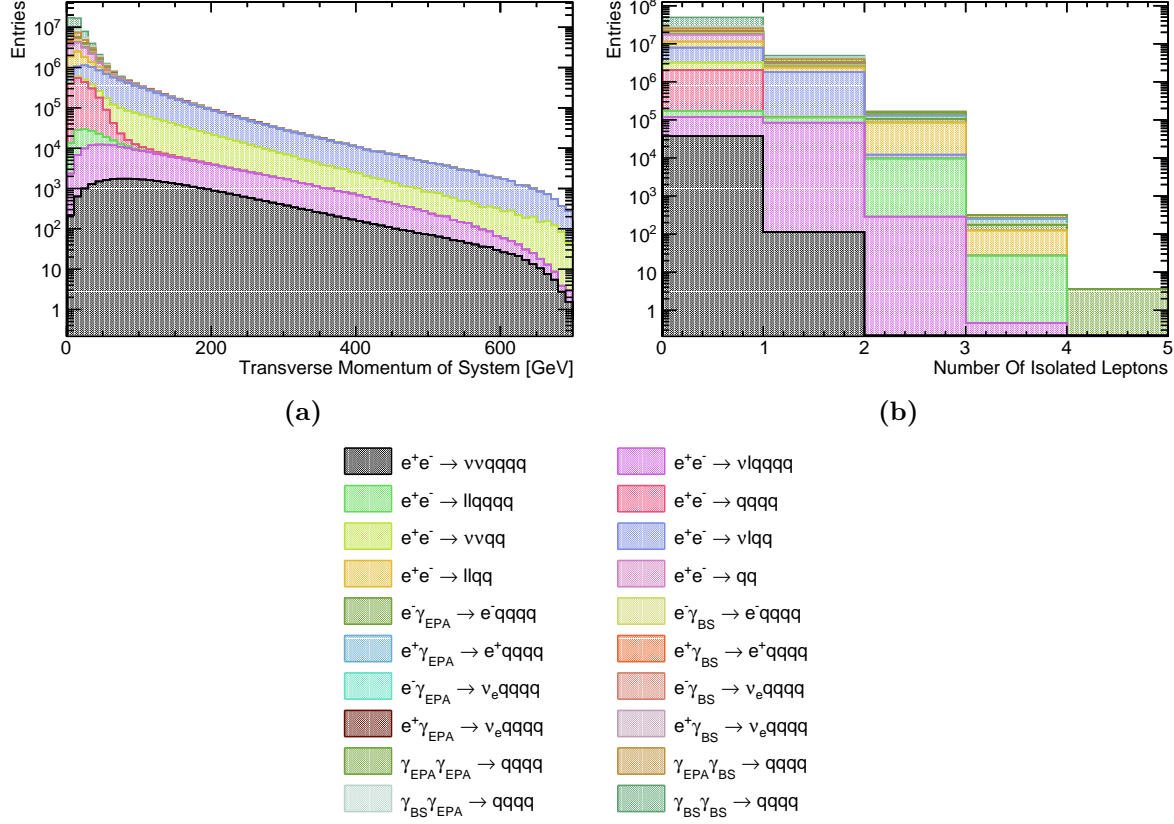


Figure 2.8: Distribution of the preselection cut variables for $\sqrt{s} = 1.4$ TeV: (a) the transverse momentum of the visible system; and (b) the number of isolated leptons in the system. All distributions are normalised to an integrated luminosity of $\mathcal{L}_{int} = 1.5 \text{ ab}^{-1}$.

of the individual decision trees. The cuts applied in the decision tree are determined using the training sample.

- ***k*-Nearest Neighbour (KNN).** For a given input event, the k closest neighbours from the training sample are found. The classifier for that input event is determined as the fraction of those k events that belong to the signal sample. Distances in this classifier are defined as the Euclidean distance between events in the n -dimensional space of the variables used for training the classifier. Weights are applied when calculating the distances to account for the differing widths of the input variable distributions. The value of k used in this analysis was 20.
- **Multilayer Perceptron (MLP).** This is an example of a neutral network. Neutral networks consist of an interconnected series of neurons each with a different response to a set of input signals. The signal for the first layer of neurons in this case are

the event variables used to train the MVA. The input signal proceeds to travel through several layers of neurons. The number of neurons in a given layer is reduced as the number of layers passed through increases until two neurons are left, one corresponding to signal and the other background. The neuron giving the larger response in the final layer determines the event classifier. The training sample is used to determine the response of each neurons in the network.

- **Fisher and H-Matrix Discriminants.** These procedures involve the calculation of a hyperplane in n -dimensional space that maximally separates signal and background events in the training sample. The location of an input event in that n -dimensional space with respect to that hyperplane determines the classifier for the event. The hyperplane is determined by maximising the differences between the means of the input event variables normalised by a measure of their spread. Both the Fisher and H-Matrix discriminants search for the hyperplane in n -dimensional space, however, the Fisher discriminant begins this procedure by transforming the input variables into a variable space with zero linear correlations.
- **Likelihood.** The likelihood is determined using the probability density function (PDF) for each of the input variables. PDFs are determined using the training sample for both signal and background events. For a given event, the likelihood is given by the product of the probability of obtaining each of the input variables for that event. The signal and background likelihoods are calculated using the signal and background PDFs respectively and the ratio of the signal likelihood to the sum of the signal and background likelihoods gives the event classifier.

The input variables used for these MVA classifiers were:

- Number of PFOs in each jet;
- Energy of the highest energy PFO;
- Energy of the highest energy electron;
- Cosine of the polar angle of the highest energy track;
- Energy of the candidate bosons;
- Invariant mass of the candidate bosons;
- Acolinearity of the candidate boson pair;
- The vector sum of the transverse momentum of all PFOs in the event;

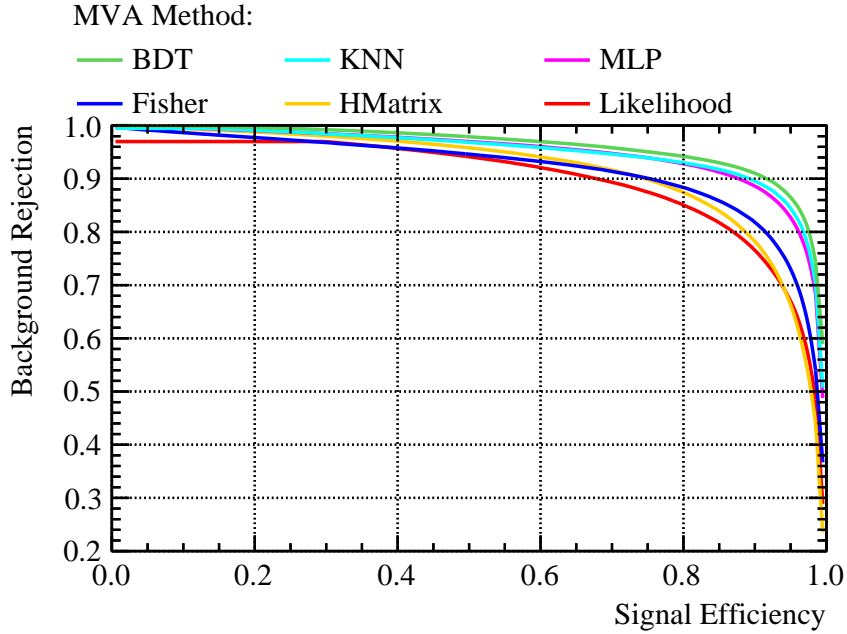


Figure 2.9: Background rejection as a function of signal efficiency for a variety of MVA options for $\sqrt{s} = 1.4$ TeV.

- The sphericity of the event;
- The derived jet clustering parameter variables $-\log_{10}(y_{ij})$ where y_{ij} are jet clustering parameters, $i = 3, 4$ and $j = i + 1$.

Figure 2.9 shows the background rejection, which is equivalent to one minus the background efficiency, as a function of signal efficiency for various MVA classifiers. Efficiency is defined as the fraction of events classified as signal by the MVA. The efficiencies reported by TMVA are calculated after the application of the preselection cuts, which are described in section 2.5.1.

The classifier giving the optimal performance in terms of signal efficiency and background rejection was the BDT. The performance of the BDT was optimised further by varying the number of trees used and the depth of the trees. An optimal significance, $S/\sqrt{S+B}$, where S and B are the number of signal and background events passing the preselection respectively, of 52.7 was obtained using the optimised BDT.

2.5.3 Event Selection Summary

The event selection is summarised using the distribution of the invariant mass of the candidate bosons, which for the signal final state should peak around the W mass. This distribution is shown in figure 2.10 with: no event selection; with the preselection cuts applied; and with both preselections cuts and MVA applied. The event selection efficiencies are also summarised in table 2.5.

As expected the dominant background processes after the MVA is applied are those that have the same topology as the signal process, i.e. four primary quarks with missing energy. Two smaller sources of background are also present: two jet events with missing energy that are confused with four jet events with missing energy and events where a lepton is not properly reconstructed causing the event to look like four jets and missing energy.

2.6 Anomalous Coupling Fitting Methodology

This section describes the procedure used for constructing the χ^2 surface and the subsequent confidence contours used to determine the sensitivity of CLIC to the anomalous gauge couplings α_4 and α_5 .

2.6.1 Sensitive Distribution

The sensitivity of CLIC to the anomalous gauge couplings will be determined through the use of a χ^2 fit. Three variables showing sensitivity to the anomalous gauge couplings were considered for use in the χ^2 fit:

- M_{VV} . The invariant mass of the visible system;
- $\cos\theta_{Bosons}^*$. The angle between the boost direction and the back-to-back candidate bosons in the rest frame of the visible system;
- $\cos\theta_{Jets}^*$. The angle between the boost direction and the back-to-back jets in the rest frame of the candidate bosons. As each event contains two candidate bosons, there are two $\cos\theta_{Jets}^*$ variables per event.

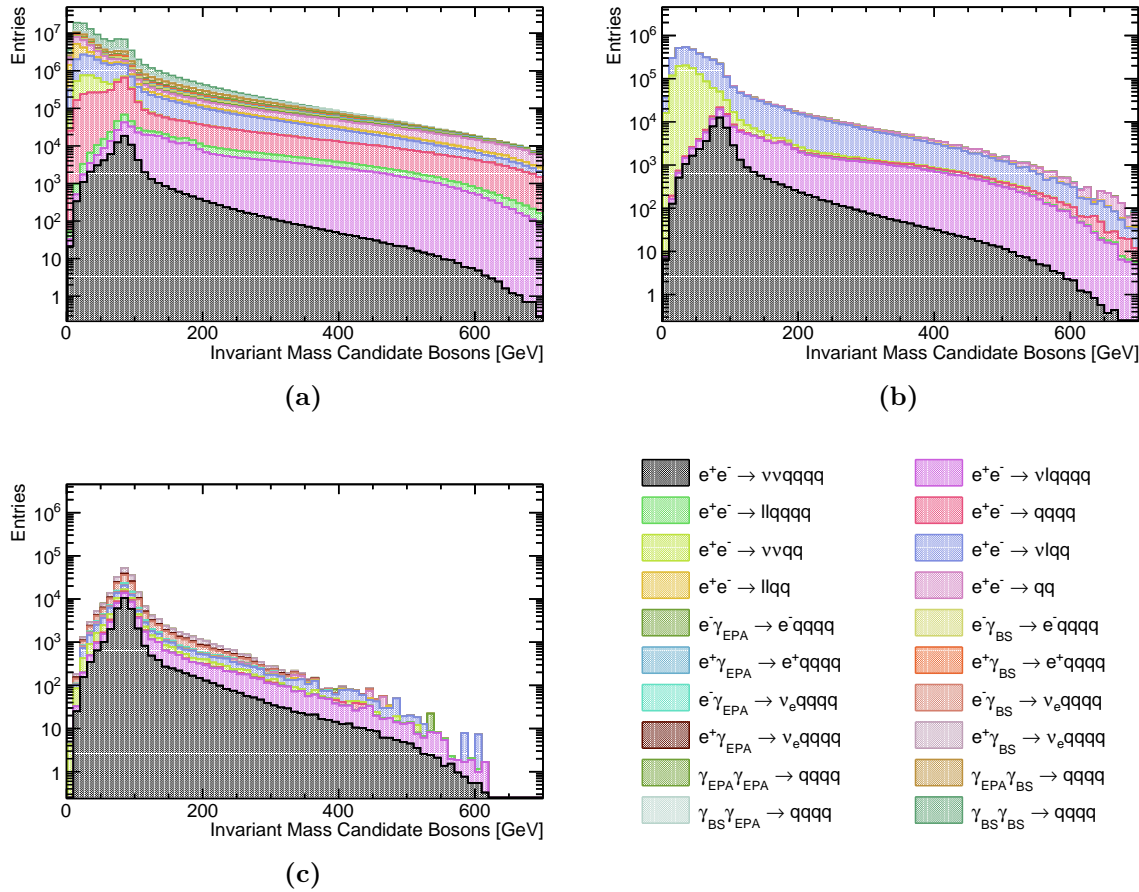


Figure 2.10: Impact of preselection and MVA on the reconstructed invariant mass of the candidate bosons for $\sqrt{s} = 1.4$ TeV: (a) no cuts; (b) after preselection; and (c) after preselection and MVA. All distributions correspond to an integrated luminosity of $\mathcal{L}_{int} = 1.5 \text{ ab}^{-1}$.

Final State	ϵ_{presel}	ϵ_{BDT}	N_{BDT}
$e^+e^- \rightarrow \nu\nuqqqq$	64.1%	44.5%	16,470
$e^+e^- \rightarrow \nu lqqqq$	26.1%	5.2%	8,582
$e^+e^- \rightarrow llqqqq$	0.8%	0.1%	100
$e^+e^- \rightarrow qqqq$	0.3%	0.1%	1,698
$e^+e^- \rightarrow \nu\nuqq$	43.4%	0.5%	5,351
$e^+e^- \rightarrow \nu lqq$	19.1%	0.1%	9,319
$e^+e^- \rightarrow llqq$	0.1%	-	234
$e^+e^- \rightarrow qq$	0.6%	-	1,586
$e^-\gamma_{\text{EPA}} \rightarrow e^-qqqq$	0.2%	-	48
$e^-\gamma_{\text{BS}} \rightarrow e^-qqqq$	0.1%	-	42
$e^+\gamma_{\text{EPA}} \rightarrow e^+qqqq$	0.3%	-	19
$e^+\gamma_{\text{BS}} \rightarrow e^+qqqq$	-	-	65
$e^-\gamma_{\text{EPA}} \rightarrow \nu_e qqqq$	26.0%	9.0%	4,421
$e^-\gamma_{\text{BS}} \rightarrow \nu_e qqqq$	36.1%	15.0%	23,150
$e^+\gamma_{\text{EPA}} \rightarrow \bar{\nu}_e qqqq$	25.9%	9.2%	4,495
$e^+\gamma_{\text{BS}} \rightarrow \bar{\nu}_e qqqq$	36.4%	15.3%	23,410
$\gamma_{\text{EPA}}\gamma_{\text{EPA}} \rightarrow qqqq$	0.2%	-	81
$\gamma_{\text{EPA}}\gamma_{\text{BS}} \rightarrow qqqq$	0.1%	-	55
$\gamma_{\text{BS}}\gamma_{\text{EPA}} \rightarrow qqqq$	-	-	53
$\gamma_{\text{BS}}\gamma_{\text{BS}} \rightarrow qqqq$	-	-	0

Table 2.5: Event selection efficiencies for $\sqrt{s} = 1.4$ TeV. In the above table, ϵ_{presel} denotes the number of events passing the preselection as a fraction of the total number of events, while ϵ_{BDT} denotes the number of events passing both the preselection and the BDT as a fraction of the total number of events. The EPA and BS subscript on the incoming photon indicates whether the photon is generated from the equivalent photon approximation or beamstrahlung. Entries with a dash indicate an efficiency of less than 0.1%. The event numbers correspond to an integrated luminosity of $\mathcal{L}_{\text{int}} = 1.5 \text{ ab}^{-1}$.

Figure 2.11 shows the distribution of these variables for the $\nu\nuqqqq$ final state for selected values of the anomalous gauge couplings α_4 and α_5 . A χ^2 fit to each of these variables was applied to obtain confidence limits on the sensitivity of CLIC to the anomalous gauge couplings, as described in section 2.6.2. The distributions used for the χ^2 fit contained signal and background events that passed event selection. Table 2.6 shows the one σ confidence limits on the measurement of α_4 and α_5 obtained using

each of the variables considered. The M_{VV} distribution shows the greatest sensitive to the anomalous gauge couplings; therefore, it will be used by all subsequent χ^2 fits when reporting sensitivities. This distribution shows the greatest sensitivity of the variables considered because the couplings primarily affect events with large values of M_{VV} and there are relatively few of these events.

Sensitive Variable	One σ Confidence Limits
M_{VV}	$-0.0082 < \alpha_4 < 0.0116$ $-0.0055 < \alpha_5 < 0.0078$
$\cos\theta_{Bosons}^*$	$-0.0111 < \alpha_4 < 0.0155$ $-0.0082 < \alpha_5 < 0.0110$
$\cos\theta_{Jets}^*$	$-0.0100 < \alpha_4 < 0.0142$ $-0.0070 < \alpha_5 < 0.0098$

Table 2.6: One σ confidence limits on the measurement of α_4 and α_5 obtained at $\sqrt{s} = 1.4$ TeV. These sensitivities include the affect from backgrounds and event selection.

2.6.2 χ^2 Surface and Confidence Limit Definition

A χ^2 surface was used to determine confidence limits on the anomalous gauge couplings given the null hypothesis that $\alpha_4 = \alpha_5 = 0$. This surface is defined as

$$\chi^2 = \sum_i \frac{(O_i - E_i)^2}{E_i}, \quad (2.9)$$

where O_i is the observed, $\alpha_4 = \alpha_5 = 0$, and E_i the expected, $\alpha_4 \neq 0$ and $\alpha_5 \neq 0$, bin content for bin i in the distribution of interest. The summation Σ_i runs over bins in the distribution of interest.

When applying the χ^2 fit to the M_{VV} distribution, the distribution was binned using 13 bins as shown in figure 2.12. The first bin spanned the invariant mass range between 0 GeV and 200 GeV, this was followed by 11 bins of width 100 GeV ranging from 200 GeV to 1300 GeV and finally the last bin contained all invariant masses above 1300 GeV. The expanded bin widths at the tails of the distribution were chosen to ensure the bin contents were sufficiently large to give a reliable estimate the likelihood function using the χ^2 parameter. This choice of bin width also ensured the bin contents were sufficiently large to minimise fluctuations arising from individual events with large weights. When applying

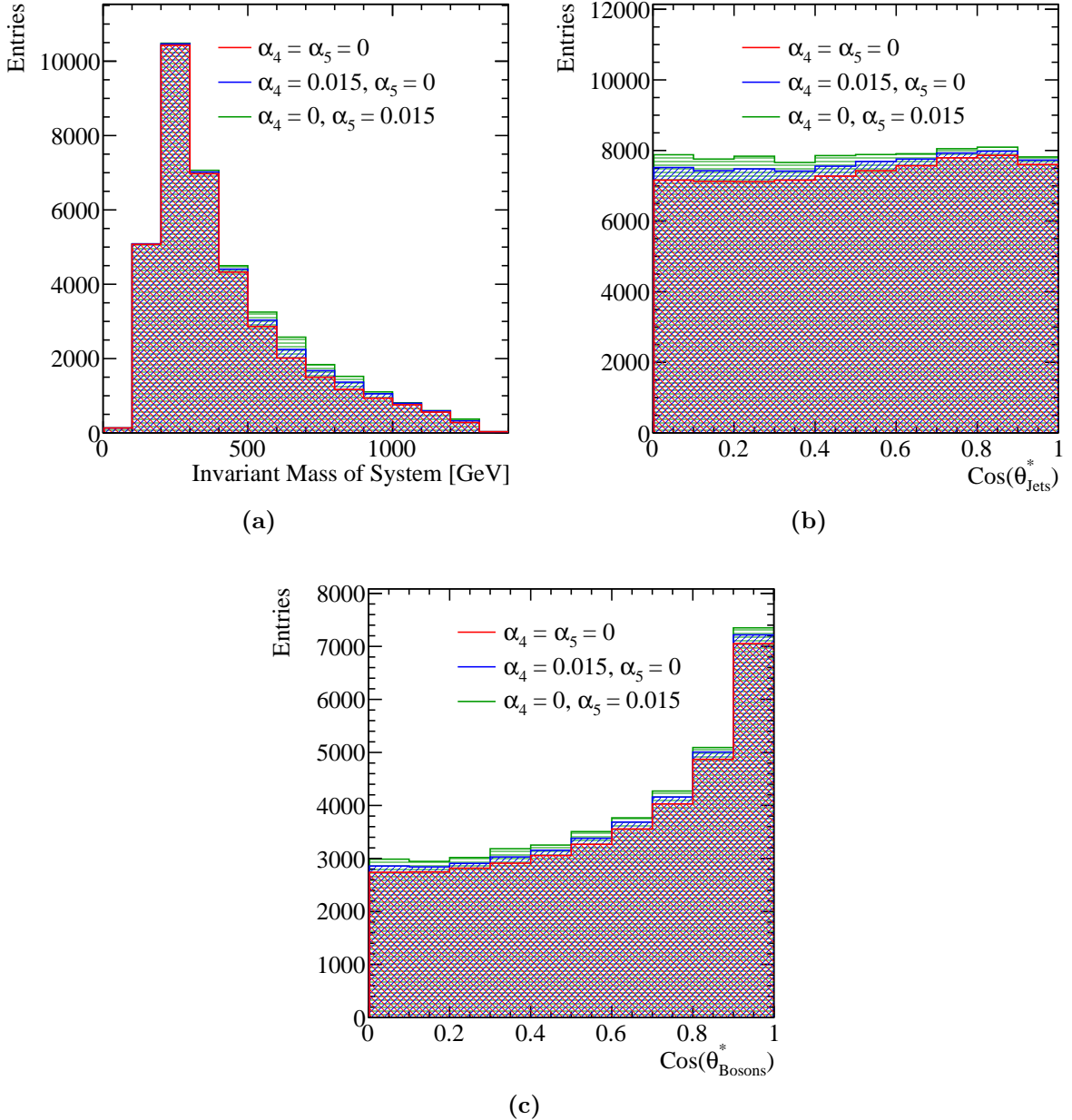


Figure 2.11: The distributions of (a) M_{VV} , (b) $\cos\theta_{\text{jets}}^*$ and (c) $\cos\theta_{\text{Bosons}}^*$ for selected values of the anomalous gauge couplings α_4 and α_5 for the $\nu\nu qqqq$ final state for $\sqrt{s} = 1.4 \text{ TeV}$. The jet algorithm used was the longitudinally invariant k_t algorithm with an R parameter of 0.9 and Selected PFOs. All distributions are normalised to an integrated luminosity of $\mathcal{L}_{int} = 1.5 \text{ ab}^{-1}$.

the χ^2 fit to distributions of the $\cos\theta_{\text{Bosons}}^*$ and $\cos\theta_{\text{jets}}^*$ variables, the distributions were binned using 10 bins ranging from zero to one. As there are two $\cos\theta_{\text{jets}}^*$ variables per event, the χ^2 fit was applied to a two dimensional distribution of $\cos\theta_{\text{jets}}^*$, where

a distinction between the two $\cos\theta_{Jets}^*$ variables was made based on the energy of the candidate bosons. The use of a two dimensional distribution in the χ^2 fit was needed to account for any correlation between the two $\cos\theta_{Jets}^*$ variables.

Confidence limits describing the sensitivity of the CLIC experiment to the anomalous gauge couplings were found by examining the χ^2 surface in the space of α_4 and α_5 . Deviations from the minima of this surface, which by construction occurs at $\alpha_4 = \alpha_5 = 0$, yield confidence limits that indicate the probability of observing a particular value of α_4 and α_5 given the null hypothesis that $\alpha_4 = \alpha_5 = 0$. The confidence limits reported in subsequent sections, 68%, 90% and 99%, are defined using fixed deviations from the minima of χ^2 surface ($\Delta\chi^2$) of 2.28, 4.61 and 9.21 respectively.

Confidence limits on the individual parameters α_4 and α_5 were determined by setting the corresponding coupling term to zero and examining the remaining one dimensional χ^2 distribution. A fourth order polynomial was fitted to the minima of this distribution and the one sigma confidence limit defined using $\Delta\chi^2 = 1$. The definition of a one sigma confidence limit accounts for changes in the number of degrees of freedom in the fit, therefore, it changes when fixing the corresponding coupling term to zero.

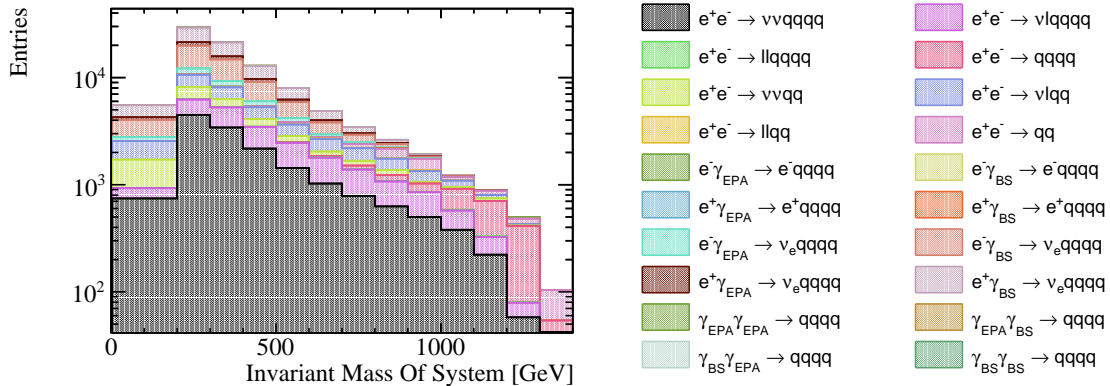


Figure 2.12: The distribution of the invariant mass of the system for both signal and background final states that is used in the χ^2 fit for $\sqrt{s} = 1.4$ TeV. The distribution includes effect of event selection and corresponds to an integrated luminosity of $\mathcal{L}_{int} = 1.5 \text{ ab}^{-1}$.

2.6.3 Event Weight Interpolation Scheme

In order to obtain a smooth χ^2 surface a fine sampling of the event weights in the α_4 and α_5 space is required, however, it is unfeasible to generate a finely sampled grid of event

weights on an event by event basis because event generation is highly CPU intensive. To resolve this issue, an interpolation scheme was applied to determine the event weights within a sampled region of the α_4 and α_5 space. This allows for an infinite sampling of the event weights in the space of α_4 and α_5 without having to call the generator an infinite number of times.

A bicubic interpolation scheme, cubic interpolation along the two dimensions, was applied to the event weights produced by the generator. This procedure is best illustrated by figure 2.13, which shows the interpolated event weight surface superimposed with the raw event weights from the generator for four $\nu\nu\text{qqqq}$ events for $\sqrt{s} = 1.4$ TeV. This interpolation scheme produces a smooth and continuous surface that can be used for generating a smooth χ^2 surface.

2.7 Results

The sensitivity of the CLIC experiment to the anomalous gauge couplings α_4 and α_5 for $\sqrt{s} = 1.4$ TeV is shown in figure 2.14a. This result shows the sensitivity after the application of preselection and MVA purposed to remove the included background channels. These contours yield the one σ confidence limits for CLIC operating for $\sqrt{s} = 1.4$ TeV of

$$-0.0082 < \alpha_4 < 0.0116, \quad (2.10)$$

$$-0.0055 < \alpha_5 < 0.0078. \quad (2.11)$$

2.7.1 Systematic Uncertainties

A source of systematic error in this experiment is the uncertainty on the cross-sections for the signal and background processes. Based on the event selection summary shown in table 2.5, the dominant source of background in this analysis comes from the $e^\pm\gamma_{\text{BS}} \rightarrow \nu_e\text{qqqq}$ processes. Therefore, uncertainties on the cross-section for these processes, as well as the signal process $e^+e^- \rightarrow \nu\nu\text{qqqq}$, will be considered.

The uncertainty on the cross-section for a given process is included in the χ^2 definition through the use of a nuisance parameter. This procedure allows the cross-section for a process to fluctuate, however, the magnitude of the fluctuation, r , is moderated by an

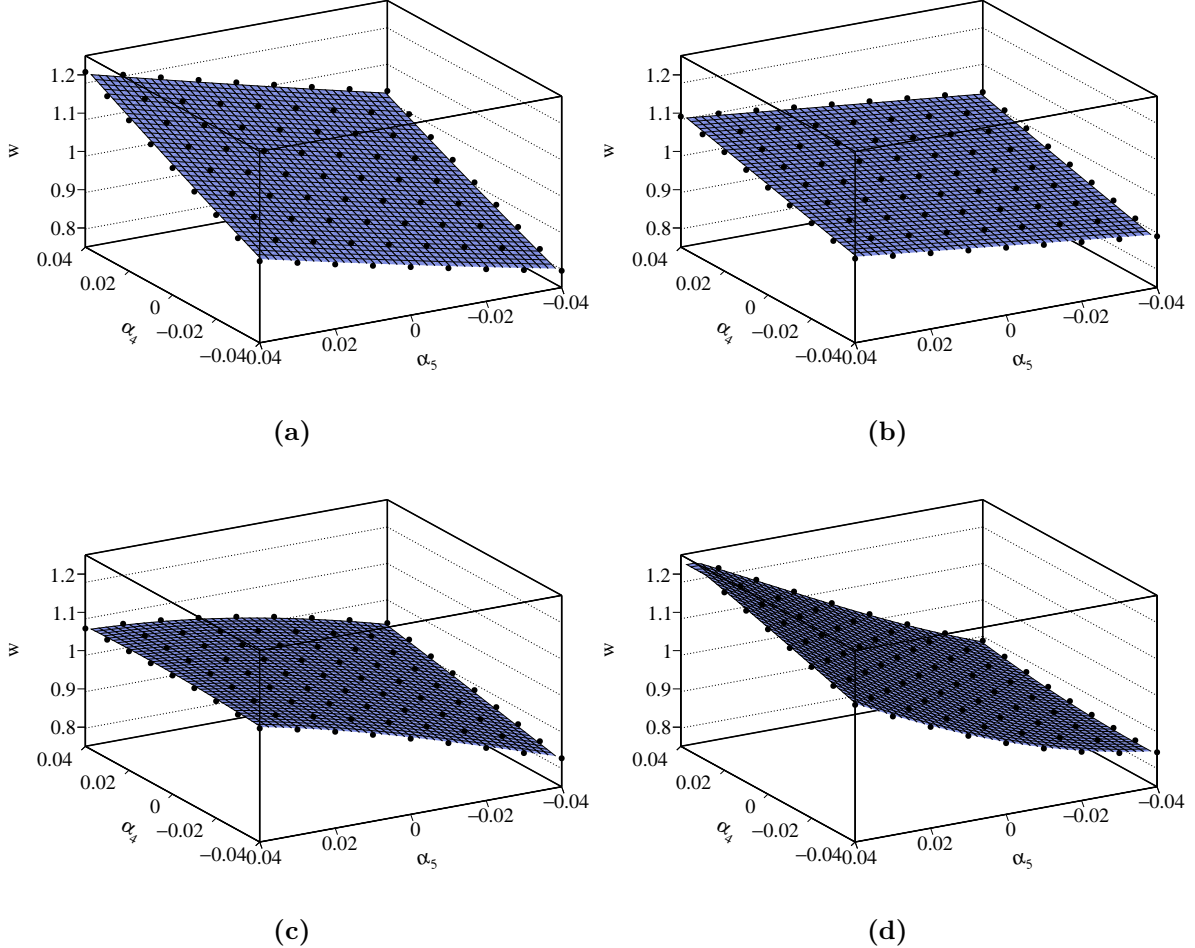


Figure 2.13: The event weight, w , as a function of the anomalous couplings α_4 and α_5 for a selection of $\sqrt{s} = 1.4$ TeV $\nu\nu\text{qqqq}$ final state events. The black circles show the event weight produced from the generator and the blue surface is determined using bicubic interpolation between these points.

additional penalty term in the χ^2 as follows

$$\chi^2(r) = \sum_i \frac{(O_i - E_i(r))^2}{E_i(r)} + \frac{(r - 1)^2}{\sigma_r^2}, \quad (2.12)$$

where O_i is the observed, $\alpha_4 = \alpha_5 = 0$, bin content for bin i in the distribution of M_{VV} with no background fluctuations and $E_i(r)$ is the expected, $\alpha_4 \neq 0$ and $\alpha_5 \neq 0$, bin content for bin i in the distribution of M_{VV} where the cross-section for the process of interest has been fluctuated by the factor r . The sum \sum_i runs over the bins in the M_{VV} distribution. The σ_r variable is the width of the distribution of r , which indicates

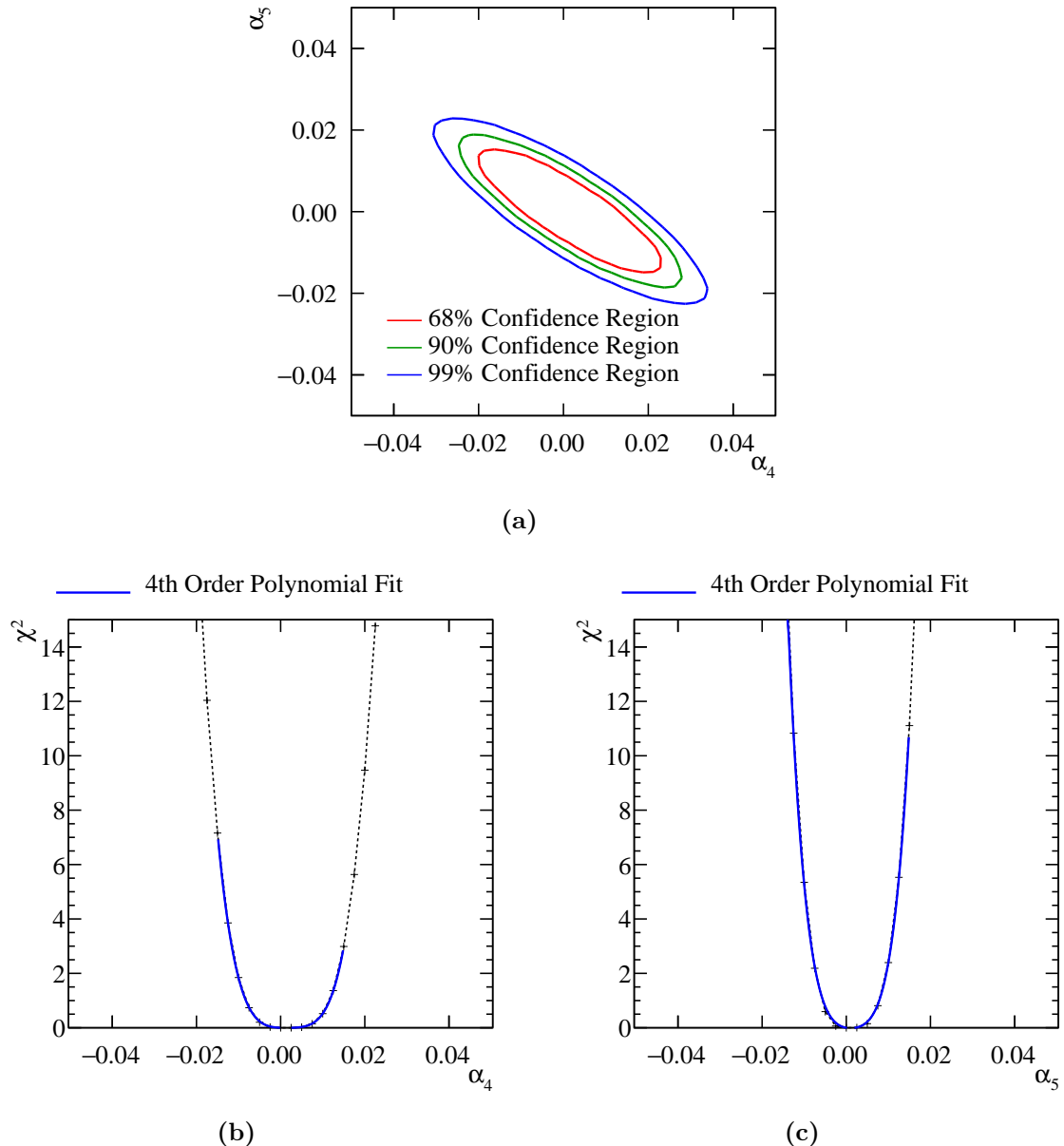


Figure 2.14: χ^2 sensitivity distributions from a fit to M_{VV} for $\sqrt{s} = 1.4$ TeV. Results include the effect of backgrounds after the application of a series of preselection cuts and MVA. (a) χ^2 sensitivity contours in α_4 and α_5 space. (b) χ^2 as a function of α_4 assuming $\alpha_5 = 0$. (c) χ^2 as a function of α_5 assuming $\alpha_4 = 0$.

the uncertainty on the measurement of the cross-section of interest. A χ^2 surface is constructed in the space of α_4 and α_5 by minimising $\chi^2(r)$ at each point.

The 68% confidence region is shown with the inclusion of a nuisance parameter for the signal process $e^+e^- \rightarrow \nu\nu qqqq$ and the dominant background processes $e^\pm \gamma_{\text{BS}} \rightarrow \nu_e qqqq$

in figures 2.15a and 2.15b respectively. Minimal changes in sensitivity are observed when allowing the signal and dominant backgrounds to fluctuate. This can be understood by considering the shape of the M_{VV} distribution for the signal and dominant background processes, which is shown in figure 2.16. These distribution shows that anomalous couplings primarily affect events with large invariant masses, while both the signal and dominant backgrounds peak at low invariant masses. Therefore, by fluctuating the cross-section for the signal and dominant background processes, it is not possible to gain a significantly better match between the observed and expected bin contents in the M_{VV} distribution. This is encouraging as despite the $e^\pm \gamma_{BS} \rightarrow \nu_e qqqq$ backgrounds dominating the χ^2 fit that determines the sensitivity of CLIC to the anomalous gauge couplings, precise knowledge of their cross-section is not crucial. As the uncertainty on these cross-sections does not significantly affect the confidence regions, no cross-section uncertainties are accounted for when reporting the sensitivity of CLIC to the anomalous gauge couplings elsewhere in this analysis.

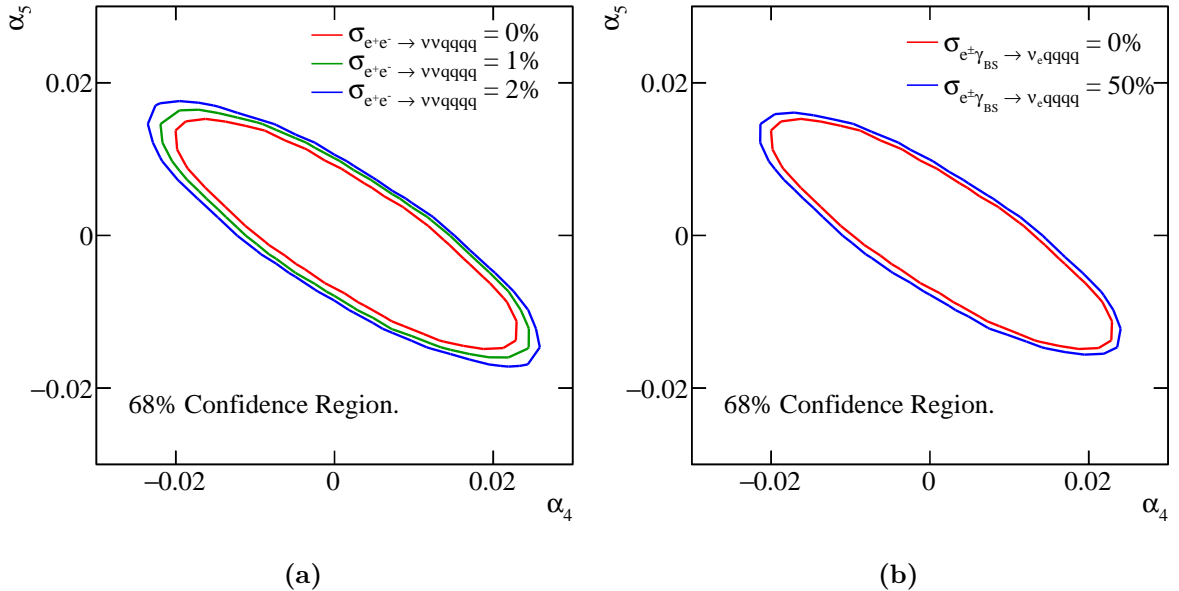


Figure 2.15: The 68% confidence region including the effect of uncertainties in the cross-section for (a) the signal process $e^+e^- \rightarrow \nu\nu qqqq$ and (b) the dominant background processes $e^\pm \gamma_{BS} \rightarrow \nu_e qqqq$.

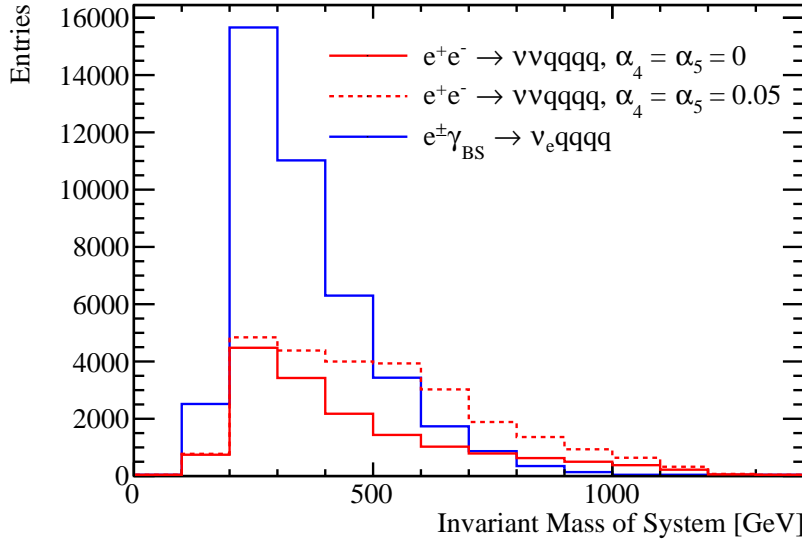


Figure 2.16: Distributions of M_{VV} for the $e^+e^- \rightarrow \nu\nu\text{qqqq}$ signal process, with and without the effect from anomalous couplings, and the combined dominant background processes $e^\pm\gamma_{BS} \rightarrow \nu_e\text{qqqq}$. All distributions include the effect of event selection and correspond to an integrated luminosity of $\mathcal{L}_{int} = 1.5 \text{ ab}^{-1}$.

2.8 Sensitivity for $\sqrt{s} = 3 \text{ TeV}$

The anomalous gauge coupling sensitivity study described in this chapter was repeated for CLIC operating for $\sqrt{s} = 3 \text{ TeV}$. As this analysis largely mirrors that of the $\sqrt{s} = 1.4 \text{ TeV}$ analysis, this section focuses on the differences between the two analyses.

The signal and background final states for the $\sqrt{s} = 3 \text{ TeV}$ analysis were identical to those used for the $\sqrt{s} = 1.4 \text{ TeV}$ analysis. Cross sections for these processes for $\sqrt{s} = 3 \text{ TeV}$ are given in table 2.7. The data analysis and event selection procedures used for $\sqrt{s} = 3 \text{ TeV}$ mirrored those used for $\sqrt{s} = 1.4 \text{ TeV}$.

Jet finding was performed using the longitudinally invariant k_t algorithm as described in section 2.4.2. The jet algorithm configuration was optimised using the sensitivity of CLIC to the anomalous gauge couplings using pure signal only, as described in section 2.4.2.1. The optimal jet algorithm configuration for $\sqrt{s} = 3 \text{ TeV}$ used tight selected PFOs and an R parameter of 1.1. As the cross-section for the $\gamma\gamma \rightarrow \text{hadrons}$ increases with energy, the effect of these background is more problematic for $\sqrt{s} = 3 \text{ TeV}$ than for $\sqrt{s} = 1.4 \text{ TeV}$ [2]. Therefore, it is to be expected that the optimal PFO selection for

Final State	Cross Section [fb]
$e^+e^- \rightarrow \nu\nuqqqq$	71.5
$e^+e^- \rightarrow \nu lqqqq$	106.6
$e^+e^- \rightarrow llqqqq$	169.3
$e^+e^- \rightarrow qqqq$	546.5
$e^+e^- \rightarrow \nu\nuqq$	1317.5
$e^+e^- \rightarrow \nu lqq$	5560.9
$e^+e^- \rightarrow llqq$	3319.6
$e^+e^- \rightarrow qq$	2948.9
$e^-\gamma_{\text{EPA}} \rightarrow e^-qqqq$	287.8
$e^-\gamma_{\text{BS}} \rightarrow e^-qqqq$	1268.6
$e^+\gamma_{\text{EPA}} \rightarrow e^+qqqq$	287.8
$e^+\gamma_{\text{BS}} \rightarrow e^+qqqq$	1267.3
$e^-\gamma_{\text{EPA}} \rightarrow \nu_e qqqq$	54.2
$e^-\gamma_{\text{BS}} \rightarrow \nu_e qqqq$	262.5
$e^+\gamma_{\text{EPA}} \rightarrow \bar{\nu}_e qqqq$	54.2
$e^+\gamma_{\text{BS}} \rightarrow \bar{\nu}_e qqqq$	262.3
$\gamma_{\text{EPA}}\gamma_{\text{EPA}} \rightarrow qqqq$	402.7
$\gamma_{\text{EPA}}\gamma_{\text{BS}} \rightarrow qqqq$	2423.1
$\gamma_{\text{BS}}\gamma_{\text{EPA}} \rightarrow qqqq$	2420.6
$\gamma_{\text{BS}}\gamma_{\text{BS}} \rightarrow qqqq$	13050.3

Table 2.7: Cross sections of signal and background processes for $\sqrt{s} = 3$ TeV. In the above table q represents u, \bar{u} , d, \bar{d} , s, \bar{s} , c, \bar{c} , b or \bar{b} ; l represents e^\pm , μ^\pm or τ^\pm ; and ν represents ν_e , $\bar{\nu}_e$, ν_μ , $\bar{\nu}_\mu$, ν_τ and $\bar{\nu}_\tau$. The EPA and BS subscript on the incoming photon indicates whether the photon is generated from the equivalent photon approximation or beamstrahlung.

$\sqrt{s} = 3$ TeV, tight selected PFOs, is more aggressive at vetoing these backgrounds than for $\sqrt{s} = 1.4$ TeV, selected PFOs, which is what is observed.

As opposed to training the MVA using 50% of the signal and background events, as was done for the $\sqrt{s} = 1.4$ TeV analysis, the $\sqrt{s} = 3$ TeV analysis trained the MVA using 10% of the signal and background events. This modification prevented those events with very large event weights from dominating the χ^2 fit and producing exaggerated sensitivities. The sensitivity to the anomalous gauge couplings grows with increasing centre of mass energy, therefore, for $\sqrt{s} = 1.4$ TeV very large event weights were not an

issue. The sample sizes for all signal and background processes was sufficiently large that training on 10% of the total sample was sufficient to achieve good MVA performance. Event selection for the $\sqrt{s} = 3$ TeV analysis is summarised in table 2.8.

Final State	ϵ_{presel}	ϵ_{BDT}	N_{BDT}
$e^+e^- \rightarrow \nu\nu qqqq$	74.4%	46.0%	65,740
$e^+e^- \rightarrow \nu lqqqq$	40.0%	12.0%	25,660
$e^+e^- \rightarrow llqqqq$	7.5%	1.1%	3,570
$e^+e^- \rightarrow qqqq$	3.7%	0.3%	3,224
$e^+e^- \rightarrow \nu\nu qq$	50.5%	1.2%	30,510
$e^+e^- \rightarrow \nu lqq$	32.0%	0.4%	48,320
$e^+e^- \rightarrow llqq$	1.4%	-	1,028
$e^+e^- \rightarrow qq$	1.4%	0.1%	3,268
$e^- \gamma_{\text{EPA}} \rightarrow e^- qqqq$	6.6%	0.8%	4,736
$e^- \gamma_{\text{BS}} \rightarrow e^- qqqq$	4.6%	0.7%	13,660
$e^+ \gamma_{\text{EPA}} \rightarrow e^+ qqqq$	6.5%	0.8%	4,686
$e^+ \gamma_{\text{BS}} \rightarrow e^+ qqqq$	4.7%	0.7%	13,310
$e^- \gamma_{\text{EPA}} \rightarrow \nu_e qqqq$	45.6%	17.2%	18,610
$e^- \gamma_{\text{BS}} \rightarrow \nu_e qqqq$	55.9%	26.7%	110,900
$e^+ \gamma_{\text{EPA}} \rightarrow \bar{\nu}_e qqqq$	45.9%	17.3%	18,750
$e^+ \gamma_{\text{BS}} \rightarrow \bar{\nu}_e qqqq$	56.5%	27.4%	113,700
$\gamma_{\text{EPA}} \gamma_{\text{EPA}} \rightarrow qqqq$	5.3%	0.7%	5,531
$\gamma_{\text{EPA}} \gamma_{\text{BS}} \rightarrow qqqq$	3.5%	0.4%	16,640
$\gamma_{\text{BS}} \gamma_{\text{EPA}} \rightarrow qqqq$	3.5%	0.4%	15,900
$\gamma_{\text{BS}} \gamma_{\text{BS}} \rightarrow qqqq$	0.6%	-	4,124

Table 2.8: Event selection efficiencies for $\sqrt{s} = 3$ TeV. In the above table, ϵ_{presel} denotes the number of events passing the preselection as a fraction of the total number of events, while ϵ_{BDT} denotes the number of events passing both the preselection and the BDT as a fraction of the total number of events. The EPA and BS subscript on the incoming photon indicates whether the photon is generated from the equivalent photon approximation or beamstrahlung. Entries with a dash indicate an efficiency of less than 0.1%. The event numbers correspond to an integrated luminosity of $\mathcal{L}_{\text{int}} = 2 \text{ ab}^{-1}$.

Due to the increased sensitivity of the signal sample, event weights were sampled with greater frequency in the space of α_4 and α_5 for $\sqrt{s} = 3$ TeV than for $\sqrt{s} = 1.4$ TeV analysis. Bicubic interpolation was again used to make a continuous surface for the event

weights. These event weight surfaces were then used to construct the M_{VV} distribution and the χ^2 surface used to determine the reported sensitivities. Figure 2.17 shows an example of the event weights extracted from the generator and the interpolated surface used to define the χ^2 surface as a function of α_4 and α_5 for a selected $\nu\nu\text{qqqq}$ event for $\sqrt{s} = 3$ TeV.

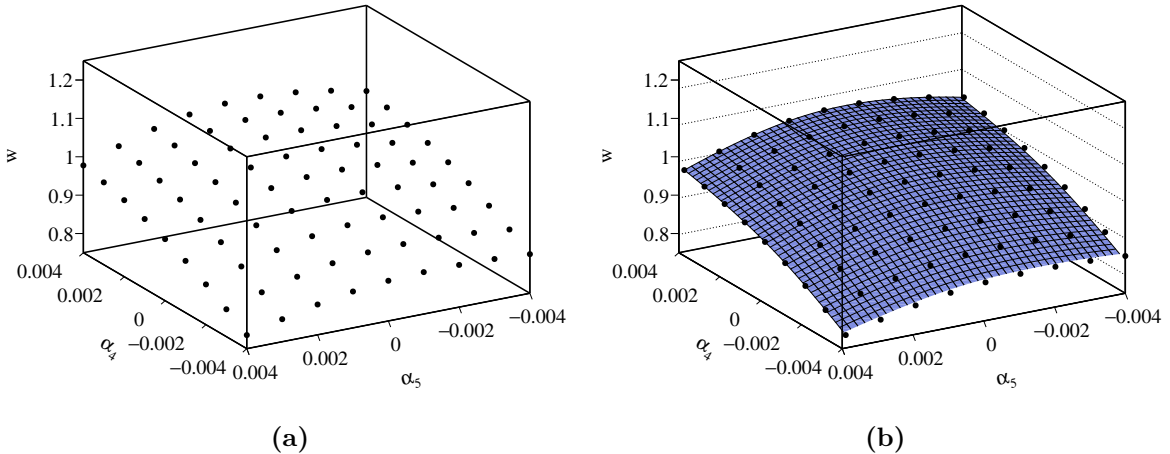


Figure 2.17: The event weights, w , as a function of the anomalous couplings α_4 and α_5 for a selected $\nu\nu\text{qqqq}$ final state events for $\sqrt{s} = 3$ TeV. These weights are calculated using (a) the generator and (b) bicubic interpolation.

A χ^2 was applied to the distribution of M_{VV} to determine the sensitivity of CLIC to the anomalous gauge couplings α_4 and α_5 for $\sqrt{s} = 3$ TeV. The M_{VV} distribution used for the fit had an increased number of bins with respect to the $\sqrt{s} = 1.4$ TeV analysis; the first bin spanned the invariant mass range between 0 GeV and 200 GeV, this was followed by 27 bins of width 100 GeV ranging from 200 GeV to 1300 GeV and finally the last bin contained all invariant masses above 2900 GeV. Figure 2.18 shows the M_{VV} distribution for signal and background processes for $\sqrt{s} = 3$ TeV that was used in the χ^2 fit.

The sensitivity of the CLIC experiment to the anomalous gauge couplings α_4 and α_5 for $\sqrt{s} = 3$ TeV is shown in figure 2.19a. This result shows the sensitivity after the application of preselection and MVA, described in sections 2.5.1 and 2.5.2, purposed to remove the included background channels. These contours yield the one σ confidence limit on the measurement of

$$-0.0010 < \alpha_4 < 0.0011, \quad (2.13)$$

$$-0.0007 < \alpha_5 < 0.0007. \quad (2.14)$$

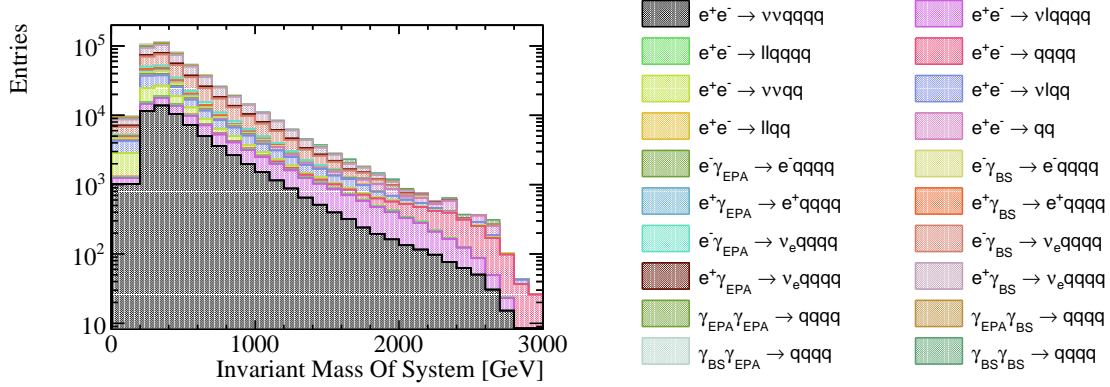


Figure 2.18: The distribution of the invariant mass of the system for both signal and background final states that is used in the χ^2 fit for $\sqrt{s} = 3$ TeV. The distribution includes effect of event selection and corresponds to an integrated luminosity of $\mathcal{L}_{int} = 2 \text{ ab}^{-1}$.

Figure 2.20 shows how the 68% confidence region for the $\sqrt{s} = 3$ TeV analysis varies with the uncertainty in the cross-section for the signal, $e^+e^- \rightarrow \nu\nu\text{qqqq}$, and dominant background processes, $e^\pm\gamma_{\text{BS}} \rightarrow \nu_e\text{qqqq}$. These contours were produced using a nuisance parameter as discussed in section 2.7.1. Once again, these systematic uncertainties have a small effect on the reported sensitivity of CLIC to the anomalous gauge couplings due to the shape of the M_{VV} distribution.

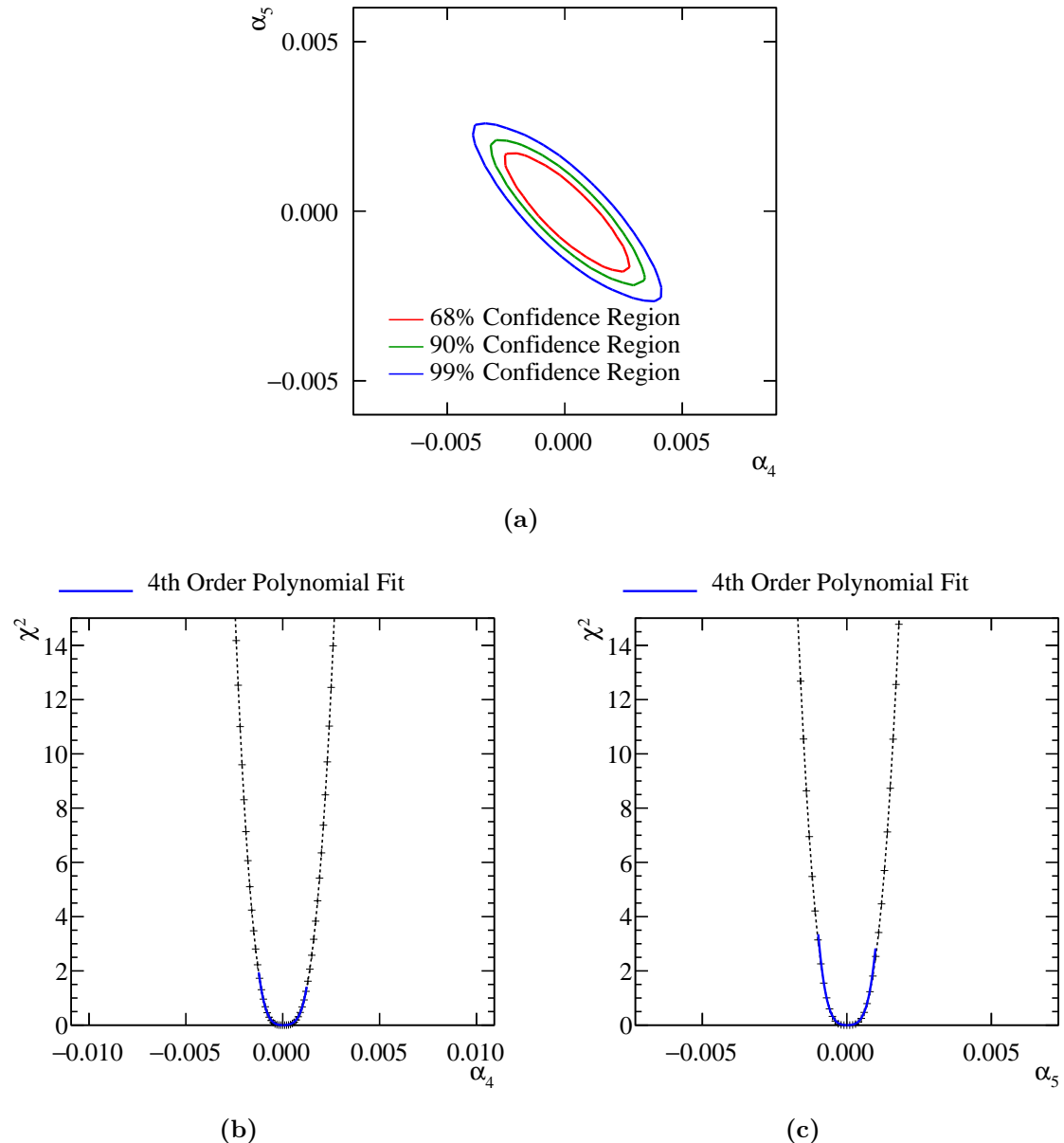


Figure 2.19: χ^2 sensitivity distributions from a fit to M_{VV} for $\sqrt{s} = 3$ TeV. Results include the effect of backgrounds after the application of a series of preselection cuts and MVA. (a) χ^2 sensitivity contours in α_4 and α_5 space. (b) χ^2 as a function of α_4 assuming $\alpha_5 = 0$. (c) χ^2 as a function of α_5 assuming $\alpha_4 = 0$.

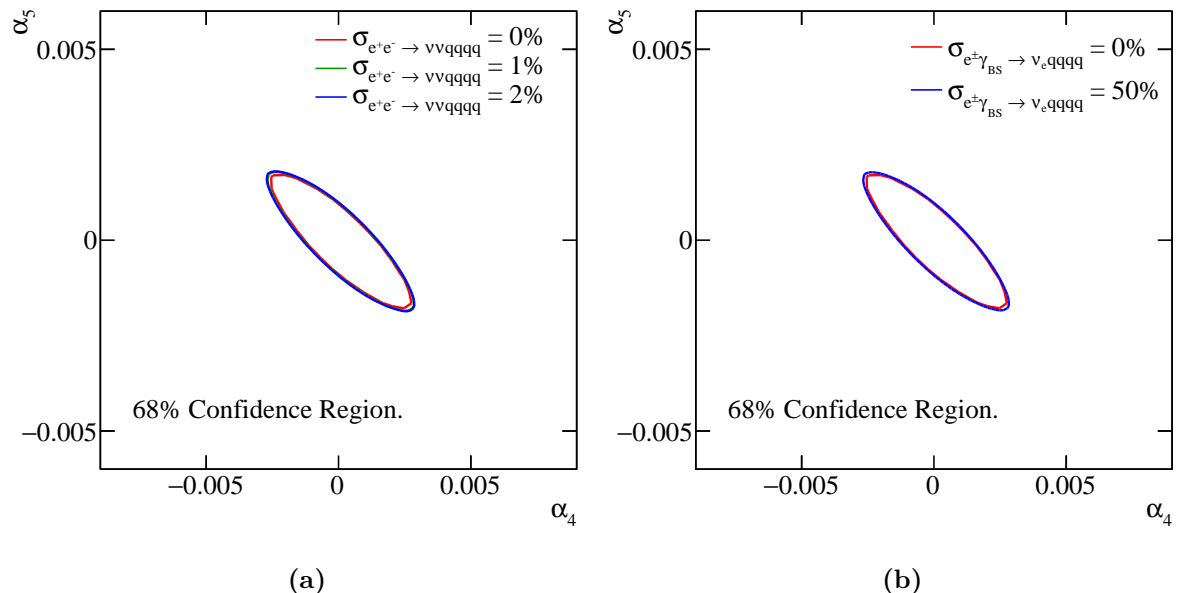


Figure 2.20: The 68% confidence region including the effect of uncertainties in the cross-section for (a) the signal process $e^+e^- \rightarrow \nu\nu qqqq$ and (b) the dominant background processes $e^\pm \gamma_{BS} \rightarrow \nu_e qqqq$.

Colophon

This thesis was made in L^AT_EX 2 _{ε} using the “heptesis” class [45].

Bibliography

- [1] M. A. Thomson. Particle Flow Calorimetry and the PandoraPFA Algorithm. *Nucl. Instrum. Meth.*, A611:25–40, 2009.
- [2] J. S. Marshall, A. Münnich, and M. A. Thomson. Performance of Particle Flow Calorimetry at CLIC. *Nucl. Instrum. Meth.*, A700:153–162, 2013.
- [3] Halina Abramowicz et al. The International Linear Collider Technical Design Report - Volume 4: Detectors. 2013.
- [4] Toshinori Abe et al. The International Large Detector: Letter of Intent. 2010.
- [5] Serguei Chatrchyan et al. Energy Calibration and Resolution of the CMS Electromagnetic Calorimeter in pp Collisions at $\sqrt{s} = 7$ TeV. *JINST*, 8:P09009, 2013. [JINST8,9009(2013)].
- [6] M. Aharrouche et al. Energy linearity and resolution of the ATLAS electromagnetic barrel calorimeter in an electron test-beam. *Nucl. Instrum. Meth.*, A568:601–623, 2006.
- [7] Pascal Perret. First Years of Running for the LHCb Calorimeter System. *PoS*, TIPP2014:030, 2014.
- [8] Huong Lan Tran, Katja Krüger, Felix Sefkow, Steven Green, John Marshall, Mark Thomson, and Frank Simon. Software compensation in Particle Flow reconstruction. 2017.
- [9] M. Chefdeville et al. Shower development of particles with momenta from 15 GeV to 150 GeV in the CALICE scintillator-tungsten hadronic calorimeter. *JINST*, 10(12):P12006, 2015.
- [10] Howard S. Budd. CMS central hadron calorimeter. *Nucl. Phys. Proc. Suppl.*, 54B:191–197, 1997. [,191(2001)].

- [11] A. Airapetian et al. ATLAS calorimeter performance Technical Design Report. 1996.
- [12] P. Mora de Freitas and H. Videau. Detector simulation with MOKKA / GEANT4: Present and future. In *Linear colliders. Proceedings, International Workshop on physics and experiments with future electron-positron linear colliders, LCWS 2002, Seogwipo, Jeju Island, Korea, August 26-30, 2002*, pages 623–627, 2002.
- [13] S. Agostinelli et al. GEANT4: A Simulation toolkit. *Nucl. Instrum. Meth.*, A506:250–303, 2003.
- [14] J. B. Birks. Scintillations from Organic Crystals: Specific Fluorescence and Relative Response to Different Radiations. *Proc. Phys. Soc.*, A64:874–877, 1951.
- [15] Christian Grefe, S. Poss, Andre Sailer, and A. Tsaregorodtsev. ILCDIRAC, a DIRAC extension for the Linear Collider community. *J. Phys. Conf. Ser.*, 513:032077, 2014.
- [16] A. Tsaregorodtsev et al. DIRAC: A community grid solution. *J. Phys. Conf. Ser.*, 119:062048, 2008.
- [17] Lucie Linssen, Akiya Miyamoto, Marcel Stanitzki, and Harry Weerts. Physics and Detectors at CLIC: CLIC Conceptual Design Report. 2012.
- [18] Niloufar Alipour Tehrani, Jean-Jacques Blaising, Benoit Cure, Dominik Dannheim, Fernando Duarte Ramos, Konrad Elsener, Andrea Gaddi, Hubert Gerwig, Steven Green, Christian Grefe, Daniel Hynds, Wolfgang Klempt, Lucie Linssen, Nikiforos Nikiforou, Andreas Matthias Nurnberg, John Stuart Marshall, Marko Petric, Sophie Redford, Philipp Gerhard Roloff, Andre Sailer, Felix Sefkow, Eva Sicking, Nicolas Siegrist, Frank Richard Simon, Rosa Simoniello, Simon Spannagel, Szymon Krzysztof Sroka, Lars Rickard Strom, and Matthias Artur Weber. CLICdet: The post-CDR CLIC detector model. Mar 2017.
- [19] J. S. Marshall and M. A. Thomson. The Pandora Software Development Kit for Pattern Recognition. *Eur. Phys. J.*, C75(9):439, 2015.
- [20] F. Gaede. Marlin and LCCD: Software tools for the ILC. *Nucl. Instrum. Meth.*, A559:177–180, 2006.
- [21] H. Abramowicz et al. Higgs Physics at the CLIC Electron-Positron Linear Collider. 2016.
- [22] Torbjorn Sjostrand, Stephen Mrenna, and Peter Z. Skands. PYTHIA 6.4 Physics and Manual. *JHEP*, 05:026, 2006.

- [23] G. Alexander et al. A Comparison of b and u d s quark jets to gluon jets. *Z. Phys.*, C69:543–560, 1996.
- [24] Z. Was. TAUOLA the library for tau lepton decay, and KKMC / KORALB / KORALZ /... status report. *Nucl. Phys. Proc. Suppl.*, 98:96–102, 2001. [,96(2000)].
- [25] Serguei Chatrchyan et al. Measurement of the $W\gamma$ and $Z\gamma$ inclusive cross sections in pp collisions at $\sqrt{s} = 7\text{TeV}$ and limits on anomalous triple gauge boson couplings. *Phys. Rev.*, D89(9):092005, 2014.
- [26] Georges Aad et al. Measurement of W^+W^- production in pp collisions at $\sqrt{s} = 7\text{TeV}$ with the ATLAS detector and limits on anomalous WWZ and WW $\tilde{t}\tilde{t}$ couplings. *Phys. Rev.*, D87(11):112001, 2013. [Erratum: Phys. Rev.D88,no.7,079906(2013)].
- [27] Serguei Chatrchyan et al. Search for $WW\gamma$ and $WZ\gamma$ production and constraints on anomalous quartic gauge couplings in pp collisions at $\sqrt{s} = 8\text{TeV}$. *Phys. Rev.*, D90(3):032008, 2014.
- [28] C. W. Fabjan and F. Gianotti. Calorimetry for particle physics. *Rev. Mod. Phys.*, 75:1243–1286, 2003.
- [29] C. Adloff et al. Hadronic energy resolution of a highly granular scintillator-steel hadron calorimeter using software compensation techniques. *JINST*, 7:P09017, 2012.
- [30] E. Fermi. An attempt of a theory of beta radiation. 1. *Z. Phys.*, 88:161–177, 1934.
- [31] Georges Aad et al. Evidence for Electroweak Production of $W^\pm W^\pm jj$ in pp Collisions at $\sqrt{s} = 8\text{TeV}$ with the ATLAS Detector. *Phys. Rev. Lett.*, 113(14):141803, 2014.
- [32] J. Beringer et al. Review of Particle Physics (RPP). *Phys. Rev.*, D86:010001, 2012.
- [33] Wolfgang Kilian, Thorsten Ohl, and Jurgen Reuter. WHIZARD: Simulating Multi-Particle Processes at LHC and ILC. *Eur. Phys. J.*, C71:1742, 2011.
- [34] Mauro Moretti, Thorsten Ohl, and Jurgen Reuter. O'Mega: An Optimizing matrix element generator. 2001.
- [35] C. F. von Weizsacker. Radiation emitted in collisions of very fast electrons. *Z. Phys.*, 88:612–625, 1934.
- [36] E. J. Williams. Correlation of certain collision problems with radiation theory. *Kong. Dan. Vid. Sel. Mat. Fys. Medd.*, 13N4(4):1–50, 1935.

- [37] W. Kilian. WHIZARD 1.0: A generic Monte-Carlo integration and event generation package for multi-particle processes.
- [38] Matteo Cacciari, Gavin P. Salam, and Gregory Soyez. FastJet User Manual. *Eur. Phys. J.*, C72:1896, 2012.
- [39] S. Catani, Yuri L. Dokshitzer, M. H. Seymour, and B. R. Webber. Longitudinally invariant K_t clustering algorithms for hadron hadron collisions. *Nucl. Phys.*, B406:187–224, 1993.
- [40] Stephen D. Ellis and Davison E. Soper. Successive combination jet algorithm for hadron collisions. *Phys. Rev.*, D48:3160–3166, 1993.
- [41] S. Catani, Yuri L. Dokshitzer, M. Olsson, G. Turnock, and B. R. Webber. New clustering algorithm for multi - jet cross-sections in e+ e- annihilation. *Phys. Lett.*, B269:432–438, 1991.
- [42] Yuri L. Dokshitzer, G. D. Leder, S. Moretti, and B. R. Webber. Better jet clustering algorithms. *JHEP*, 08:001, 1997.
- [43] O. Wendt, F. Gaede, and T. Kramer. Event Reconstruction with MarlinReco at the ILC. *Pramana*, 69:1109–1114, 2007.
- [44] Andreas Hoecker, Peter Speckmayer, Joerg Stelzer, Jan Therhaag, Eckhard von Toerne, and Helge Voss. TMVA: Toolkit for Multivariate Data Analysis. *PoS*, ACAT:040, 2007.
- [45] Andy Buckley. The heptesis L^AT_EX class.